





# Assessing the importance of H<sub>2</sub>O content in the tectono-metamorphic evolution of shear zones: A case study from the Dora-Maira Massif (Western Alps)

Sara Nerone<sup>1</sup>  | Alessandro Petroccia<sup>1</sup>  | Fabiola Caso<sup>2</sup>  | Davide Dana<sup>1</sup>  | Andrea Maffei<sup>1</sup> 

<sup>1</sup>Dipartimento di Scienze della Terra, Università di Torino, Turin, Italy

<sup>2</sup>Dipartimento di Scienze della Terra "A. Desio", Università degli Studi di Milano, Milan, Italy

## Correspondence

Alessandro Petroccia, Dipartimento di Scienze della Terra, Università di Torino, Via Valperga Caluso 35, 10125 Turin, Italy.

Email: [alessandrogiovannimichele.petroccia@unito.it](mailto:alessandrogiovannimichele.petroccia@unito.it)

Handling Editor: Dr. Bernardo Cesare

## Abstract

Metamorphic reactions are commonly driven to completion within shear zones thanks to fluid circulation, making the re-equilibration of the mineral assemblage one of the dominant processes. Despite the important role of H<sub>2</sub>O in such processes, forward thermodynamic modelling calculations commonly assume either H<sub>2</sub>O-saturated conditions or only fluid loss during prograde evolution to peak conditions. These assumptions influence the understanding of shear zones during the retrograde evolution. Here, we investigate the *P*–*T*–*M*H<sub>2</sub>O retrograde evolution of the Mt. Bracco Shear Zone (MBSZ), an Alpine ductile tectonic contact which marks the boundary between two HP units in the Dora-Maira Massif (Western Alps, Italy). After the eclogite-facies peak (at 500–520°C and 1.8–2.2 GPa), the subsequent mylonitic event is constrained at amphibolite-facies conditions, continuing its evolution at decreasing pressure and temperature during rock exhumation, from ~590°C, 1.0 GPa down to ~520°C, 0.7 GPa. The *P*/*T*–*M*H<sub>2</sub>O forward modelling highlights different behaviour for the two analysed samples. After reaching a minimum H<sub>2</sub>O content at the transition from eclogite- to amphibolite-facies conditions, a significant fluid gain is modelled for only one of the two analysed samples just before the mylonitic event. The MBSZ then evolves towards H<sub>2</sub>O-undersaturated conditions. This work thus underlines the necessity of investigating the H<sub>2</sub>O evolution within shear zones, as the H<sub>2</sub>O content is susceptible to change through the *P*–*T* path, due to dehydration reactions or fluid infiltration events. Furthermore, lithological heterogeneities influence possible different fluid circulation regimes in shear zones, resulting in externally or internally derived fluid gain.

## KEYWORDS

fluid content, mylonites, phase equilibrium modelling, *P*–*T*–*M*H<sub>2</sub>O relations, shear zones

This is an open access article under the terms of the [Creative Commons Attribution](https://creativecommons.org/licenses/by/4.0/) License, which permits use, distribution and reproduction in any medium, provided the original work is properly cited.

© 2023 The Authors. *Journal of Metamorphic Geology* published by John Wiley & Sons Ltd.

## 1 | INTRODUCTION

During the orogenic evolution of collisional chains, shear zones accommodate displacement by localizing deformation across all scales (e.g., Carosi et al., 2020; Holyoke & Tullis, 2006; Mancktelow, 2006; Petroccia et al., 2022). Shear zones progressively reduce the mineral grain size due to protracted strain localization (Brodie & Rutter, 1987; De Bresser et al., 2001) and require the presence of weakening mechanisms (Gerbi et al., 2010; Giuntoli et al., 2020; Goncalves et al., 2016; Gueydan et al., 2014; Simonetti et al., 2021; Steffen et al., 2001). In a positive feedback loop, fine-grained reaction products related to reaction weakening could make shear zones preferential pathways for fluid transfer through Earth's crust (Beach, 1980; Fyfe et al., 1978; Getsinger et al., 2013; Jamtveit et al., 2008; Menegon et al., 2015). The preferential fluid flow during the early stage of ductile deformation induces metamorphic reactions, further localizing strain (Beach, 1980). The relationship between deformation and metamorphism is thus considered as related to the access of fluids and fluid/rock interactions (e.g., Finch et al., 2016; Goncalves et al., 2012; Luisier et al., 2023; Oliot et al., 2014; Rubie, 1986). The combination of these processes inherently makes such discontinuities a place where metamorphic reactions are more easily driven to completion, boosting the overprinting of pre-existing features (Beach, 1980; Connolly, 1997; Etheridge et al., 1983; Jamtveit et al., 2008; Rubie, 1986; Wheeler, 2014).

Since complete re-equilibration during deformation aided by fluid presence is considered the dominant petrological process in shear zones, H<sub>2</sub>O-saturated conditions (i.e., the presence of a free fluid phase inducing fluid-present metamorphism; e.g., Fyfe et al., 1978; Thompson, 1983) are usually assumed in forward thermodynamic modelling calculations. High fluid/rock ratios have been reported in retrograde shear zones (e.g., Etheridge et al., 1983; McCaig et al., 1990). However, rocks commonly experience fluid loss during increasing temperatures, which should hamper retrograde reactions and preserve the prograde assemblage (e.g., Fyfe et al., 1978; Rubie, 1986; Tenczer et al., 2006). This implies that the H<sub>2</sub>O content modelled at peak *P–T* conditions would not change during cooling (i.e., the system should remain closed during exhumation; e.g., Guiraud et al., 2001; Manzotti et al., 2022). From this, when investigating the metamorphic evolution of shear zones, the assessment of H<sub>2</sub>O content and its evolution may lead to important considerations (Ceccato et al., 2020; Connolly, 1997; Diener et al., 2016; Nerone et al., 2023; Pennacchioni & Cesare, 1997; Spruzeniece & Piazzolo, 2015; Tursi, 2022; Tursi et al., 2020, 2021;

Yardley et al., 2014). Retrograde shearing can in fact be sustained under a variety of fluid regimes, from fluid-absent (Pennacchioni & Cesare, 1997; Tenczer et al., 2006) to fluid-present (Ceccato et al., 2020; Diener et al., 2016; Etheridge et al., 1983; McCaig et al., 1990). The H<sub>2</sub>O regime is susceptible to change through time, especially during metamorphism, due to dehydration reactions or fluid infiltration events (Luisier et al., 2023; Thompson, 1983). Additionally, it is still unclear whether and how different regimes can affect the same shear zone during its history.

To assess this aim, the Mt. Bracco Shear Zone (MBSZ; Avigad et al., 2003) located in the Dora-Maira Massif (DMM, Western Alps) has been investigated through a thermodynamic modelling approach. The MBSZ marks the boundary between two major units, the monometamorphic Sanfront-Pinerolo Unit and the polymetamorphic Dora-Maira Basement Complex (Avigad et al., 2003; Michard et al., 1993). Even though several studies in the DMM attempt to constrain the deformation and timing experienced by the different units (e.g., Bonnet et al., 2022; Michard et al., 1993; Vaughan-Hammon et al., 2022; Wheeler, 1991 and references therein), the syn-exhumation metamorphic stages remain only locally constrained (e.g., the Brossasco-Isasca Unit, see Ferrando et al., 2017 for a review).

This work thus proposes (i) a *P–T* estimation for the evolution of mylonitic rocks between HP continental units of the DMM and (ii) the necessity of investigating the H<sub>2</sub>O evolution within shear zones (i.e., fluid-absent or fluid-present metamorphism; Thompson, 1983), as considering a fixed H<sub>2</sub>O amount in the thermodynamic modelling may be not representative (e.g., Tursi, 2022). The MBSZ is an example of fluid content variations within a shear zone evolution, highlighting how no univocal assumption may be accurate, as well as suggesting a partly internally derived flux.

## 2 | REGIONAL SETTING

The Western Alps formed as a result of subduction and collision between different paleogeographic domains: (i) the European paleomargin; (ii) the Briançonnais microcontinent; (iii) the Piemonte-Liguria Ocean; and (iv) the Adria microplate (Angrand & Mouthereau, 2021; Beltrando et al., 2010; Schmid & Kissling, 2000). The Dora-Maira Massif (Figure 1a), one of the Internal Crystalline Massifs, belonging to the distal part of the Briançonnais paleomargin (Ballèvre et al., 2020; Gasco et al., 2013; Sandrone et al., 1993; Schmid et al., 2017), is described as a nappe-stack made by three major units (Argand, 1934; Chopin et al., 1991; Michard, 1967;

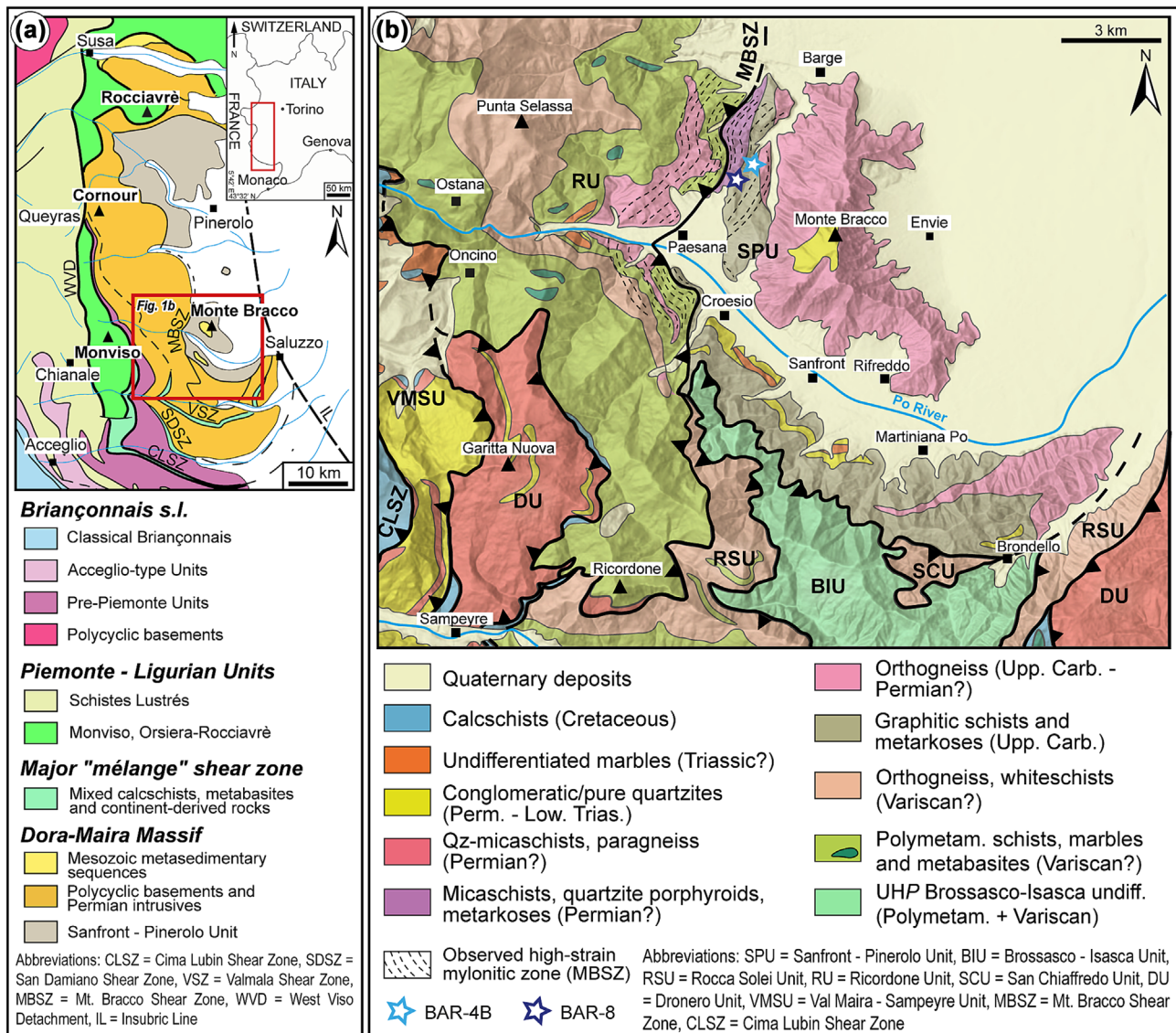


**FIGURE 1** (a) Central-Southern Western Alps simplified tectonic map highlighting the Dora-Maira Massif and surrounding areas, modified after Ballèvre et al. (2020); (b) simplified structural map of the southern Dora-Maira Massif in the Po Valley based on Vialon (1966); Crema et al. (1971); Henry (1990); Sandrone et al. (1993); Compagnoni et al. (2012); Piana et al. (2017), modified after Michard et al. (2022). The main tectonic contacts are displayed with thick black lines.

Michard et al., 1993). Moving upward, they are: (i) the Sanfront-Pinerolo Unit (SPU; Avigad et al., 2003); (ii) the Dora-Maira Basement Complex (Michard et al., 1993) and (iii) the Dronero Unit (DU; Michard et al., 2022). After structural mapping, several authors (e.g., Chopin et al., 1991; Compagnoni et al., 2012; Henry et al., 1993; Manzotti et al., 2022; Michard et al., 2022; Vialon, 1966) divided the Dora-Maira Basement Complex into minor (sub-)units (Table S1). From the structurally lower to the higher, around the investigated area they are (Figure 1b; see Michard et al., 2022 for review): (i) the Brossasco-Isasca Unit (BIU); (ii) the Rocca Solei Unit (RSU); (iii) the Ricordone Unit (RU). The monocyclic SPU has been classically associated with a blueschist-facies

metamorphic peak (Borghi et al., 1985; Vialon, 1966), while the overlying polycyclic units of the Dora-Maira Basement Complex (Nosenzo et al., 2022, 2023) reached eclogite-facies with different  $P$ - $T$  conditions (see Table S1 for more detail). Ductile tectonic contacts separate these units (Avigad, 1992; Henry et al., 1993).

The investigated shear zone, i.e., the MBSZ (Figure 1b), marks the boundary between the structurally lower SPU (Avigad et al., 2003; Chopin et al., 1991; Groppo et al., 2019) and the structurally upper RU (Henry, 1990; Michard et al., 1995). The SPU is the deepest tectonic unit of the Cottian Alps (Argand, 1911) and occurs in a similar structural position to the Money Unit belonging to the Gran Paradiso Massif (Compagnoni



et al., 1974; Le Bayon & Ballèvre, 2006; Manzotti et al., 2016). It is made up of a metasedimentary sequence which includes meta-arkose, metaconglomerates (Mertz & Siddans, 1985; Manzotti et al., 2015; Petrocchia & Iaccarino, 2021) and graphitic schists, considered the metamorphic HP equivalent of the Upper Carboniferous sequences cropping out in the Zone Houillèr (Ballèvre et al., 2020; Franchi & Novarese, 1895; Manzotti et al., 2016; Merlo & Malaroda, 1990; Vialon, 1966). The SPU is intruded by orthogneiss, supposedly derived from Permian granodiorite (Bussy & Cadoppi, 1996). Relicts of presumed Permo-Triassic cover, such as quartzites (*Bargiolina*, Cavallo & Dino, 2019; Dino et al., 2021) and marbles, are present (Michard, 1967). The structurally higher RU (Figure 1b), similarly to the other Dora-Maira Basement Complex eclogitic (sub-)units, is made up of polycyclic micaschists, gneiss, amphibolites and monocyclic orthogneiss (Sandrone et al., 1993).

Recently, Groppo et al. (2019) constrained the prograde to peak metamorphic conditions of the aforementioned units, suggesting similar burial mechanisms. Chopin et al. (1991) estimated metamorphic peak conditions near  $\sim 500^{\circ}\text{C}$  and 0.8–1.0 GPa for the SPU. According to Avigad et al. (2003), the same unit reached garnet-blueschist-facies conditions ( $\sim 500^{\circ}\text{C}$ , 1.2–1.6 GPa), whereas Groppo et al. (2019) estimated “cold” eclogite-facies conditions ( $500\text{--}520^{\circ}\text{C}$ , 2.1–2.4 GPa). Recent data from Bonnet et al. (2022) provide SPU Zr-in-rutile peak temperatures of  $\sim 513 \pm 20^{\circ}\text{C}$  (assuming pressures of 2.2 GPa). Values of  $\sim 500\text{--}600^{\circ}\text{C}$  and 0.6–0.7 GPa were estimated by Avigad et al. (2003) for the SPU retrograde path. The RU, instead, reached quartz-eclogite-facies conditions (Henry, 1990),  $\sim 1.5$  GPa and  $500\text{--}550^{\circ}\text{C}$  (Chopin et al., 1991). Slightly lower peak temperatures ( $448 \pm 20$  and  $433 \pm 34^{\circ}\text{C}$ , with assumed pressures of 2.2 GPa) were obtained by Bonnet et al. (2022), who also dated the metamorphic peak at  $40 \pm 6.2$  My for the RU. Data obtained from Zr-in-rutile thermometry on garnet-micaschist show temperatures of  $\sim 531 \pm 22$ ,  $559 \pm 18$  and  $509 \pm 24^{\circ}\text{C}$  (assuming a pressure of 0.6 GPa for the first two estimates and a pressure of 0.3 GPa for the last one) for the RU retrogression (Bonnet et al., 2022). The decompression of the DMM was associated with a retrograde path with moderate cooling followed by a reheating stage, constrained at  $500\text{--}550^{\circ}\text{C}$  and  $\sim 0.5$  GPa by garnet-biotite geothermometer and garnet-plagioclase-biotite-quartz geobarometer (Borghi et al., 1985, 1996; Sandrone & Borghi, 1992). Similar conditions have been highlighted for retrogression by Avigad et al. (2003). This metamorphic stage is characterized by the growth of a new generation of garnet and oligoclase rim around albite (Borghi et al., 1985, 1996).

### 3 | ANALYTICAL METHODS

Field and mesoscale observations have been performed along an E–W-oriented transect following the natural Po Valley from Envie to Ostana towns (Figure 1b). A non-numerical progression for the description of structural elements has been used (e.g., Sp, Sp-1). Abbreviations are: (S) for syn-metamorphic surfaces or axial plane foliation and (D) for the deformation phases. The suffix “p” denotes “principal”. Microstructural analyses were performed on oriented thin sections cut parallel to the object lineation and perpendicular to the main foliation (approximating the XZ plane of the finite strain ellipsoid). Mineral abbreviations are after Warr (2021), except for Wm, which stands for white mica. Foliations, kinematic indicators and mylonites have been classified according to Passchier and Trouw (2005). Quartz microstructures, indicative of dynamic recrystallization, are defined according to Stipp et al. (2002, 2010) and Law (2014).

#### 3.1 | Mineral chemical analysis

Petrographic identification of fine-grained minerals was performed with a Scanning Electron Microscope (SEM) JEOL JSM-IT300LV, equipped with an energy-dispersive spectrometer (EDS) Energy 200 System and an SSD X-Act3 detector (Oxford Inca Energy), hosted at the Department of Earth Sciences, University of Torino (Italy). Mineral compositions and compositional maps were obtained with an Electron Microprobe Analyzer (EMPA) JEOL 8200 Super Probe equipped with five wavelength-dispersive spectrometers (WDS) hosted at the Department of Earth Sciences “A. Desio”, University of Milano (Italy). Analytical conditions for mineral point analyses were 15 KeV accelerating voltage and 5 nA specimen current. For the acquisition of the maps, a 100 nA specimen current was used, with 30 ms of dwell time (De Andrade et al., 2006) and a pixel size of  $7 \mu\text{m}$  for the BAR-4B sample and 40 ms and  $30 \mu\text{m}$  for the BAR-8 sample. The X-ray maps of representative areas of the thin sections were processed using the program XMapTools v.4 (Lanari et al., 2014) to extract the effective bulk composition needed for the subsequent thermodynamic study. The X-ray maps were calibrated with mineral composition point analyses as internal standards for analytical standardization. Quantitative mineral chemical analyses were recalculated through the software NORM (Ulmer, 1986) to obtain chemical proportions of the rock-forming phases. Structural formulae have been calculated based on 12 oxygens for garnet, 11 for white mica, 14 for chloritoid, 8 for plagioclase, 12.5 for epidote, 11 for biotite



and 28 for chlorite.  $\text{Fe}^{3+}$  content has been calculated from stoichiometry and charge balance, while  $\text{FeO}_{\text{tot}}$  accounts for FeO and  $\text{Fe}_2\text{O}_3$ .  $X_{\text{Mg}}$  is defined as  $\text{Mg}/(\text{Mg} + \text{Fe}^{2+})$  for most minerals, while for garnet  $X_{\text{Mg}}$  is  $\text{Mg}/(\text{Mg} + \text{Fe}^{2+} + \text{Ca} + \text{Mn})$ , and  $X_{\text{Ca}}$ ,  $X_{\text{Fe}}$  and  $X_{\text{Mn}}$  are determined accordingly.  $X_{\text{An}}$  of plagioclase is defined as  $\text{An}/(\text{An} + \text{Ab} + \text{Or})$ , while  $X_{\text{Zo}}$  of epidote is defined as  $\text{Zo}/(\text{Zo} + \text{Ep} + \text{Pmt})$ . The collected mineral chemical analysis datasets of both samples are reported in Tables S2 and S3.

### 3.2 | Thermodynamic modelling

Isochemical phase diagrams to reconstruct the  $P$ - $T$  history of the MBSZ mylonites were calculated in the 10-component MnNKCFMASHT ( $\text{MnO}$ - $\text{Na}_2\text{O}$ - $\text{K}_2\text{O}$ - $\text{CaO}$ - $\text{FeO}_{\text{tot}}$ - $\text{MgO}$ - $\text{Al}_2\text{O}_3$ - $\text{SiO}_2$ - $\text{H}_2\text{O}$ - $\text{TiO}_2$ ) system with saturated  $\text{H}_2\text{O}$  using Perple\_X 6.9.1 (Connolly, 2005, 2009).  $\text{Fe}_2\text{O}_3$  was neglected in our calculations for sample BAR-4B, as in a graphite-bearing metapelite with no magnetite nor haematite, it will be present in minor amounts in the white mica and epidote (Forshaw & Pattison, 2021), thus not participating with a significant role in modelled metamorphic reactions. Due to the presence of epidote in sample BAR-8, the influence of  $\text{Fe}_2\text{O}_3$  has been investigated through the calculation of a  $P$ - $X$  ( $\text{Fe}_2\text{O}_3$ ) phase diagram at fixed  $T$ . This phase diagram has been calculated by adding epidote to the bulk rock composition, in the same pressure range of the  $P$ - $T$  phase diagrams and in an  $X$  ( $\text{Fe}_2\text{O}_3$ ) range, calculated as  $\text{Fe}_2\text{O}_3/\text{FeO}_{\text{tot}}$ , of 0–0.25. The reference  $T$  (i.e.,  $550^\circ\text{C}$ ) has been taken from the average of the range proposed by Avigad et al. (2003). Two  $P$ - $T$  isochemical phase diagrams have been computed in the range of  $400$ – $650^\circ\text{C}$  and  $0.5$ – $2.5$  GPa for sample BAR-4B considering the garnet core + mantle fractionation in the effective bulk composition extracted with XMapTools. Only one  $P$ - $T$  isochemical phase diagram was calculated for sample BAR-8, as garnet is rather homogeneous. Local bulk compositions were generated from the oxide weight-percentage maps by averaging pixels with a density correction (Lanari & Engi, 2017). For the calculations, the internally consistent thermodynamic database for condensed phases of Holland and Powell (2011) (ds62) and the equation of state for the binary fluid  $\text{H}_2\text{O}$ - $\text{CO}_2$  of Holland and Powell (1998) have been adopted. Fluid saturation conditions have been assumed with a pure  $\text{H}_2\text{O}$  fluid phase (i.e.,  $a_{\text{H}_2\text{O}} = 1$ ). The following solution models were used: garnet, chloritoid, staurolite, chlorite, white mica, biotite and ilmenite (White et al., 2014), clinopyroxene (Green et al., 2007), amphibole (Green et al., 2016), feldspar (Fuhrman & Lindsley, 1988) and in the  $P$ - $X$  ( $\text{Fe}_2\text{O}_3$ )

phase diagram also epidote (Holland & Powell, 2011). The variation in  $\text{H}_2\text{O}$  content, hereby  $\text{MH}_2\text{O}$  (i.e., the structural  $\text{H}_2\text{O}$  in the minerals plus the  $\text{H}_2\text{O}$  in the fluid, if present, in wt%; Powell et al., 2005), has been investigated through  $P$ / $T$ - $\text{MH}_2\text{O}$  phase diagrams. These are calculated along the reconstructed  $P$ - $T$  path (see Table S4 for  $P$ / $T$  gradients) in an  $\text{MH}_2\text{O}$  range of 2.5–4 wt% for BAR-4B and 0.3–1.1 wt% for BAR-8, spanning from fluid undersaturation to fluid saturation for the investigated bulk compositions.

### 4 | MESO- AND MICROSTRUCTURAL FEATURES OF THE MBSZ

The Mt. Bracco Shear Zone (MBSZ; Avigad et al., 2003) is defined by a N-S trending mylonitic zone (Figure 1b), involving both the structurally lower SPU and the higher RU (Figure 2). The mylonitic deformation increases both from the RU and the SPU toward the MBSZ (Figure 2). West of the MBSZ, deformed but non-mylonitic gneiss and micaschist of the RU unit are present (Figure 2). Graphitic schist, fine-grained meta conglomerate and meta-arkose belonging to the SPU crop out on the eastern side of the shear zone. An Sp-1 foliation has been detected in correspondence with the Fp fold hinge, far from the MBSZ (Figure 2). However, due to the strong transposition related to the subsequent phase (Dp), it is challenging to identify fold systems and foliations associated with the Dp-1. Fp folds are tight to the isoclinal. These folds deform and transpose the older Sp-1 foliation making an Sp parallel or sub-parallel to the relative fold axial planes and to the boundary of the MBSZ, representing the main foliation at the outcrop scale. The strike of the Sp foliation is relatively constant, ranging from N-S to NW-SE, dipping mainly towards W-SW, with local variations. The occurrence of the kinematic indicators increases toward the centre of the MBSZ and the mylonitic foliation becomes more pervasive (Figure 2). Thus, approaching the centre of the MBSZ, considering the differences in rheological behaviour between lithologies, the shear-related deformation increases (Figure 2) and contemporaneously, folds become tighter and rare. In gneissic mylonites, the foliation is an anastomosing disjunctive foliation (Passchier & Trouw, 2005) formed by alternating coarse-grained layers of deformed quartz-feldspar and thin mica-rich layers. In the mylonitic schists, a variation from a disjunctive foliation with sub-parallel foliation domains to a continuous schistosity is observable. White mica, chlorite and rare biotite generally mark the main foliation (Sp; Figure 2). The Sp foliation wraps around garnet and plagioclase, showing a sporadic internal foliation (Sp-1)



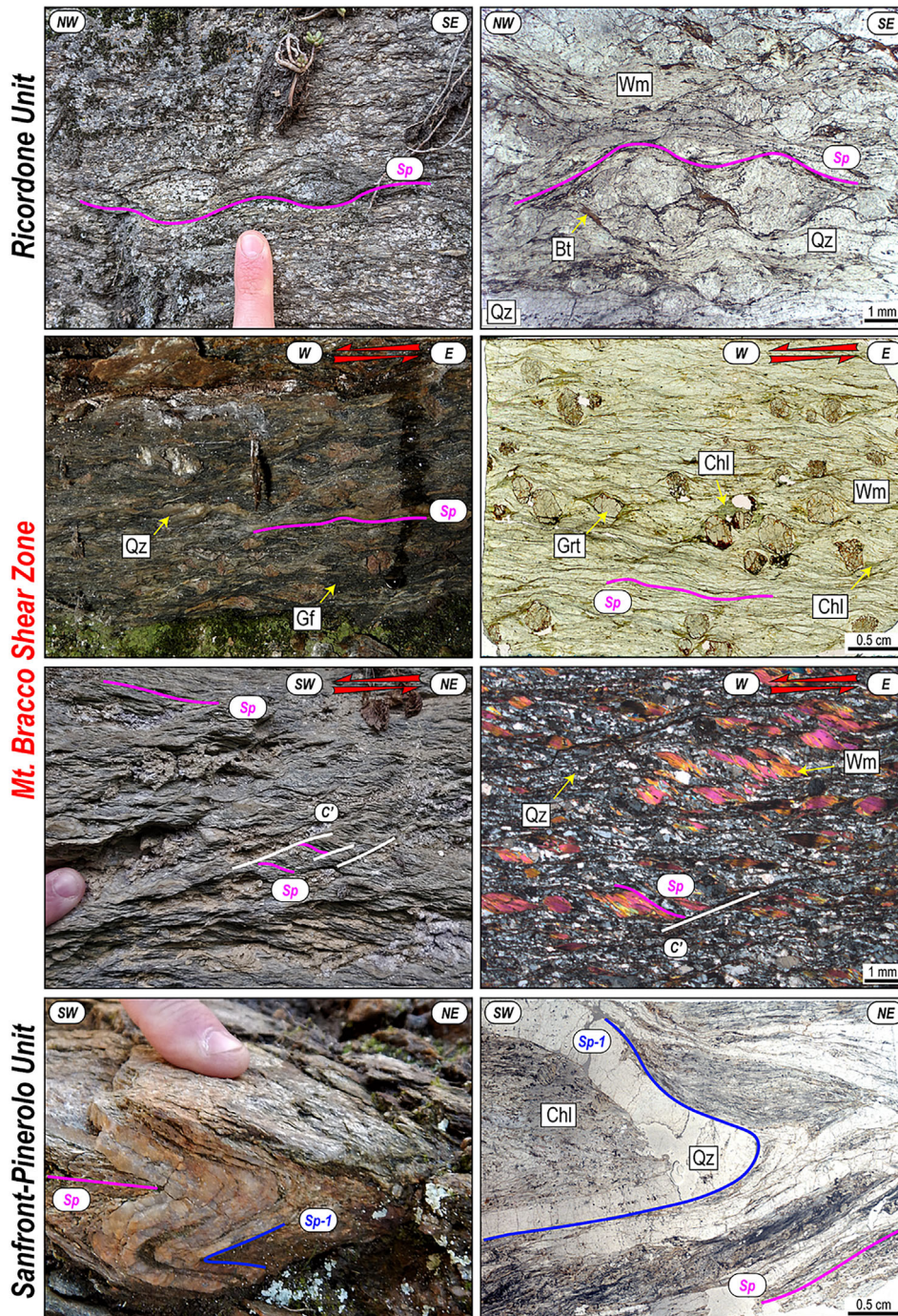


**FIGURE 2** Deformation features of RU, SPU and the MBSZ affecting both units. Meso- and micro-scale evidence of the increase in kinematic indicators (e.g., rotated porphyroblasts, S-C' fabric, mica-fish) going toward the MBSZ from both units.

that varies from discordant to concordant with the external one. Microstructural relations suggest that both garnet and plagioclase could be pre- to syn-tectonic with respect to the Dp event. Kinematic indicators (e.g., S-C and S-C' fabric, mica-fish and quartz oblique foliation; Figure 2), both at meso- and micro-scale, indicate a top-to-the W sense of shear, with local variations toward SW and NW. Quartz shows flattened grains with undulose extinction surrounded by new grains, suggesting a main sub-grain rotation recrystallization mechanism (SRR) with minor effects related to grain boundary migration (GBM).

The chosen samples (BAR-4B and BAR-8; GPS coordinates  $44^{\circ}42'11.96''\text{N} - 7^{\circ}18'16.66''\text{E}$ ,  $44^{\circ}41'53.12''\text{N} - 7^{\circ}18'6.33''\text{E}$ , respectively) are mylonites belonging to the shear-deformed SPU located within the eastern sector of the MBSZ. After carefully investigating more than 40 thin sections, these 2 samples were selected as the most representative of the shear deformation related to the MBSZ and one of them shows a mineral assemblage (e.g., multistage garnet, chloritoid, biotite) helpful for the estimation of the HP conditions (BAR-4B).



## 5 | PETROGRAPHY, MICROSTRUCTURES AND MINERAL CHEMISTRY

Samples BAR-4B and BAR-8 (see Figure 1b for location) are garnet-plagioclase-bearing rocks with a marked mylonitic fabric (Figure 3a,b).

Sample BAR-4B is a micaschist, while sample BAR-8 is a quartz-rich gneiss. Following the bulk chemical classification SandClass3 of Herron (1988), sample BAR-4B protolith was a shale, not far from the Worldwide Average Pelite (Forshaw & Pattison, 2023), while sample BAR-8 protolith was a lith-arenite (Figure S1). In both samples, the main foliation (Sp) is defined by the preferred orientation of mm-thick layers of white mica, chlorite, minor biotite and ilmenite alternated with quartz-rich layers, which are thicker in BAR-8

(Figure 3b). BAR-4B contains mm-sized plagioclase and garnet porphyroblasts, whereas BAR-8 shows pluri-mm plagioclase porphyroblasts and sub-mm garnet crystals. Quartz mainly shows evidence of SRR with local GBM and is lately affected by local bulging (BLG). Plagioclase porphyroblasts are partially wrapped and locally in continuity with the Sp (Figure 4a,b). Garnet grains are mainly found along the Sp (Figure 4c), but BAR-4B shows garnet also included in plagioclase porphyroblasts (Figure 4d) and/or partially wrapped by the Sp. A relict Sp-1 foliation made by white mica, quartz and rutile can sometimes be recognized as internal foliation in plagioclase porphyroblasts, discordant with respect to the Sp (Figure 4a,d). White mica, rutile and chloritoid, as well as biotite, are locally observed in different microchemical domains of garnet porphyroblasts, but only in sample BAR-4B (Figure 4e,f). BAR-8 also contains epidote,

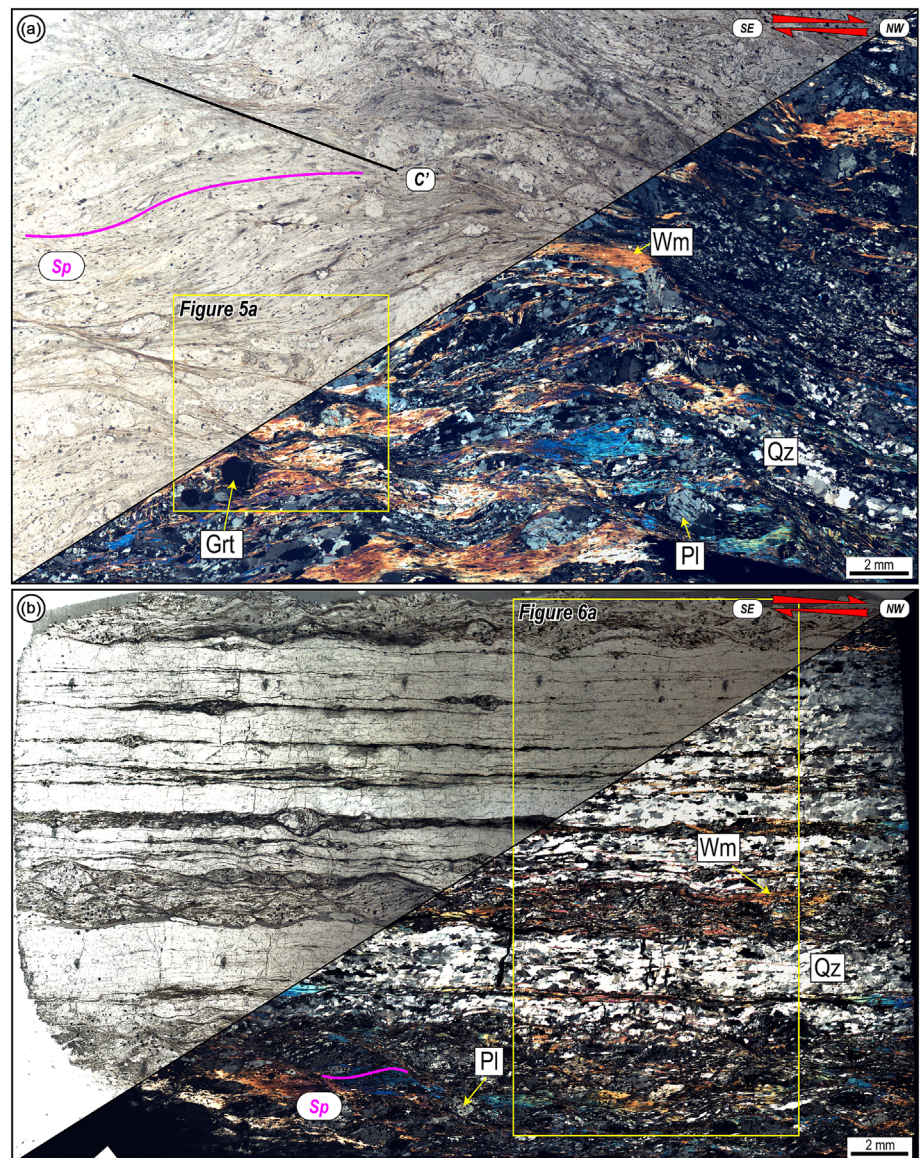


**FIGURE 3** Thin section scans of the analysed samples (a) BAR-4B and (b) BAR-8, showing a well-developed mylonitic fabric (half left is PPL: plane-polarized light; half right is XPL: crossed-polarized light). The microprobe-mapped areas have been highlighted in both samples with yellow boxes.



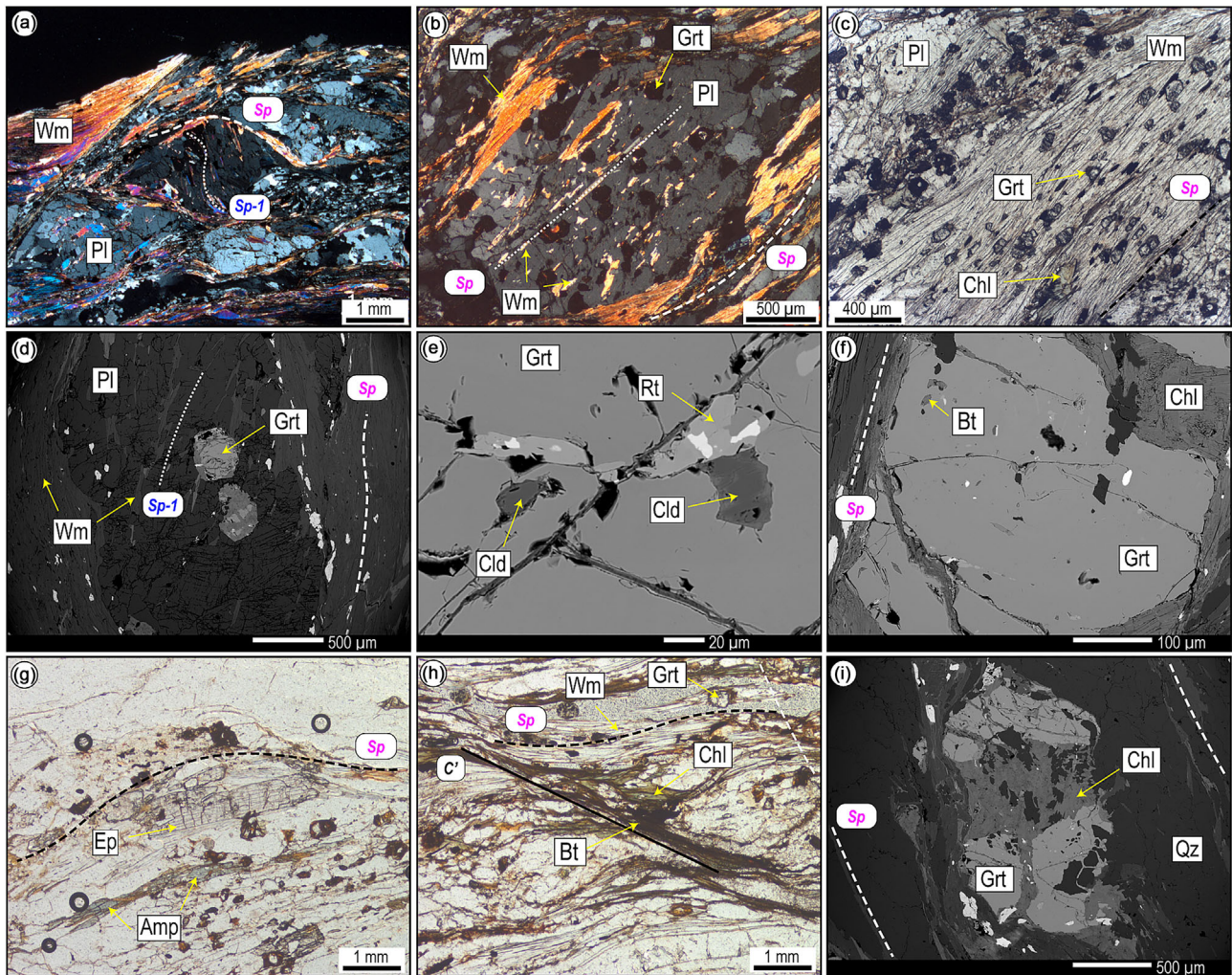


**FIGURE 4** (a) Plagioclase porphyroblasts showing an internal foliation Sp-1 discordant with respect to the external Sp, mainly marked by white mica (sample BAR-4B; XPL); (b) plagioclase porphyroblast showing an internal foliation mainly defined by white mica and sub-mm garnet in continuity with the external Sp (sample BAR-8; XPL); (c) small garnet grains along the main foliation Sp and late chlorite statically growing on the Sp (sample BAR-8; PPL); (d) garnet and white mica included within plagioclase (sample BAR-4B; BSE: back-scattered electron image); (e) chloritoid and rutile inclusions within garnet (sample BAR-4B; BSE); (f) biotite included in garnet (sample BAR-4B; BSE); (g) epidote and relict amphibole grains wrapped by the Sp foliation (sample BAR-8; PPL); (h) C' plane highlighted by biotite and subsequently substituted by chlorite (sample BAR-8; PPL); (i) fractured garnet porphyroblast replaced by chlorite (sample BAR-4B; BSE).

wrapped by the main foliation and characterized by an allanitic core, and a few relict light blue amphibole grains (Figure 4g). Chlorite defines the Sp in both samples, substituting biotite and garnet (Figure 4h,i), but also grows statically on the Sp together with white mica (Figure 4c).

Figures 5 and 6 display the mineral distribution maps obtained from the classification of X-ray maps and compositional evidence for samples BAR-4B and BAR-8, respectively. The mapped and analysed portion of BAR-4B (see Figure 3a for the X-ray map location) is characterized by (Figure 5a): white mica (43 vol%), quartz (20 vol%), chlorite (17 vol%), plagioclase (15 vol%), garnet

(4 vol%), with rutile, ilmenite and apatite as the main accessory minerals (~ 1 vol% in total). The mapped and analysed portion of BAR-8 (see Figure 3b for the X-ray map location) is characterized by (Figure 6a): quartz (65 vol%), plagioclase (16 vol%), white mica (10 vol%), chlorite (6 vol%), garnet (1 vol%), epidote (1 vol%), with rutile, ilmenite and apatite as the main accessory minerals (~ 1 vol% in total). The full dataset of mineral chemical analysis for the main phases is reported in Tables S2–S3, whereas Tables 1 and 2 present a selection of representative chemical analyses for the two samples. The chemical spot analyses (Tables S2 and S3), integrated with the minimum and maximum groups obtained from



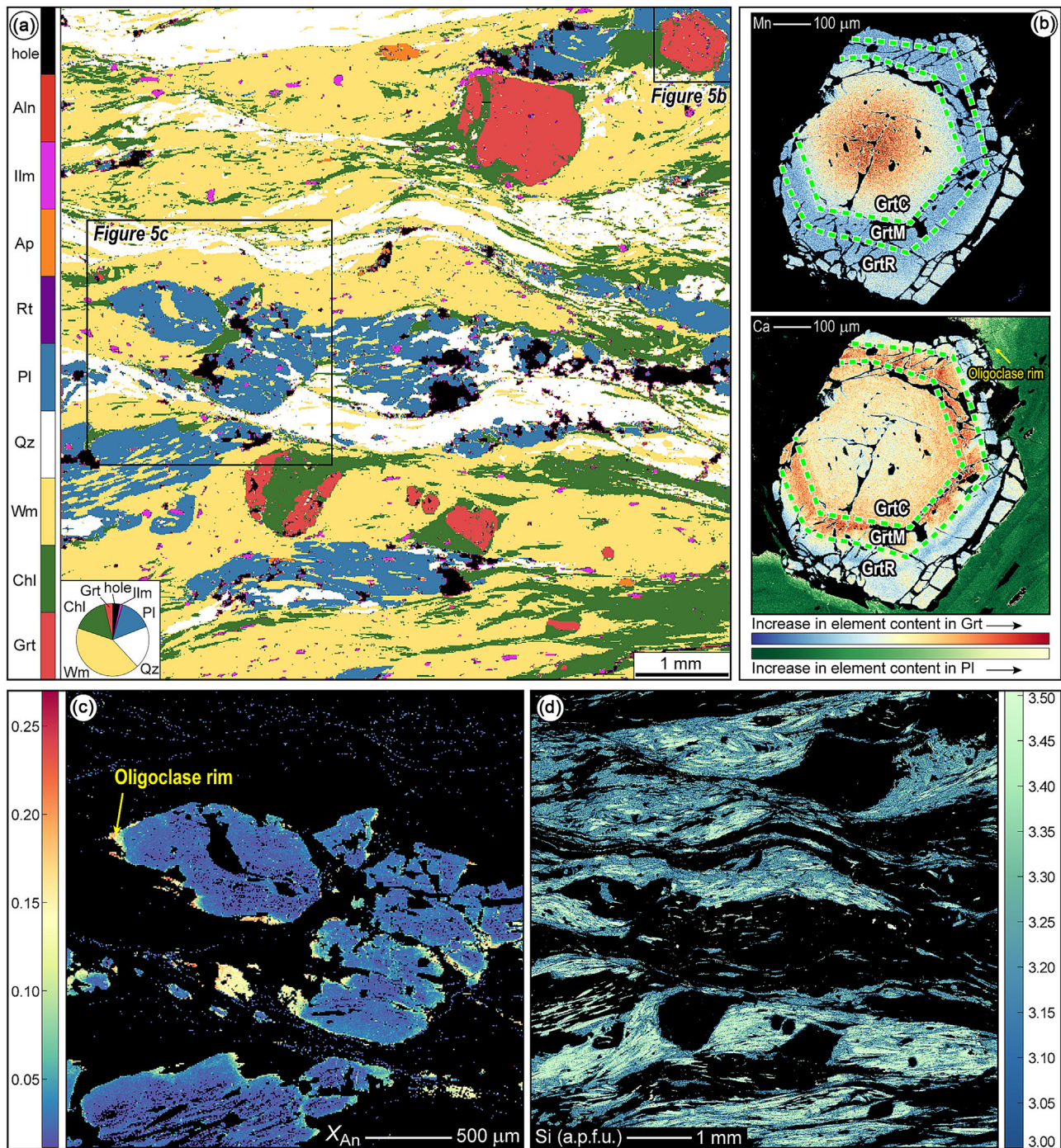


**FIGURE 5** (a) Classified X-ray map of a selected microdomain of sample BAR-4B showing the distribution and abundance of the mineralogical phases; (b) X-ray compositional maps of Mn and Ca content in garnet, as well as Ca content in plagioclase, displaying the chemical variation in garnet shells; (c)  $X_{An}$  map of plagioclase porphyroblasts, showing oligoclase rims around albite; (d) Si (a.p.f.u.) content map of white mica highlighting its compositional variation with the high-Si content white mica generally in the core of lepidoblasts.

the calibrated X-ray maps were used to define the compositional range of the different phases. See Supplementary Information S1 for the phase relation summary where pre- to post-Dp stages have been defined by microstructural relations and chemistry. Inferred blastesis-deformation relationships are summarized in Figure 7.

Garnet porphyroblasts show a well-developed chemical zoning in BAR-4B (Figure 5b) that defines a core (GrtC), a mantle (GrtM) and a rim (GrtR). Garnet is characterized by (Figures 5b and S2): (i) an increase in Ca content from the core ( $X_{Ca} = 0.14\text{--}0.19$ ) to the mantle ( $X_{Ca} = 0.17\text{--}0.22$ ), which decreases to the inner rim then



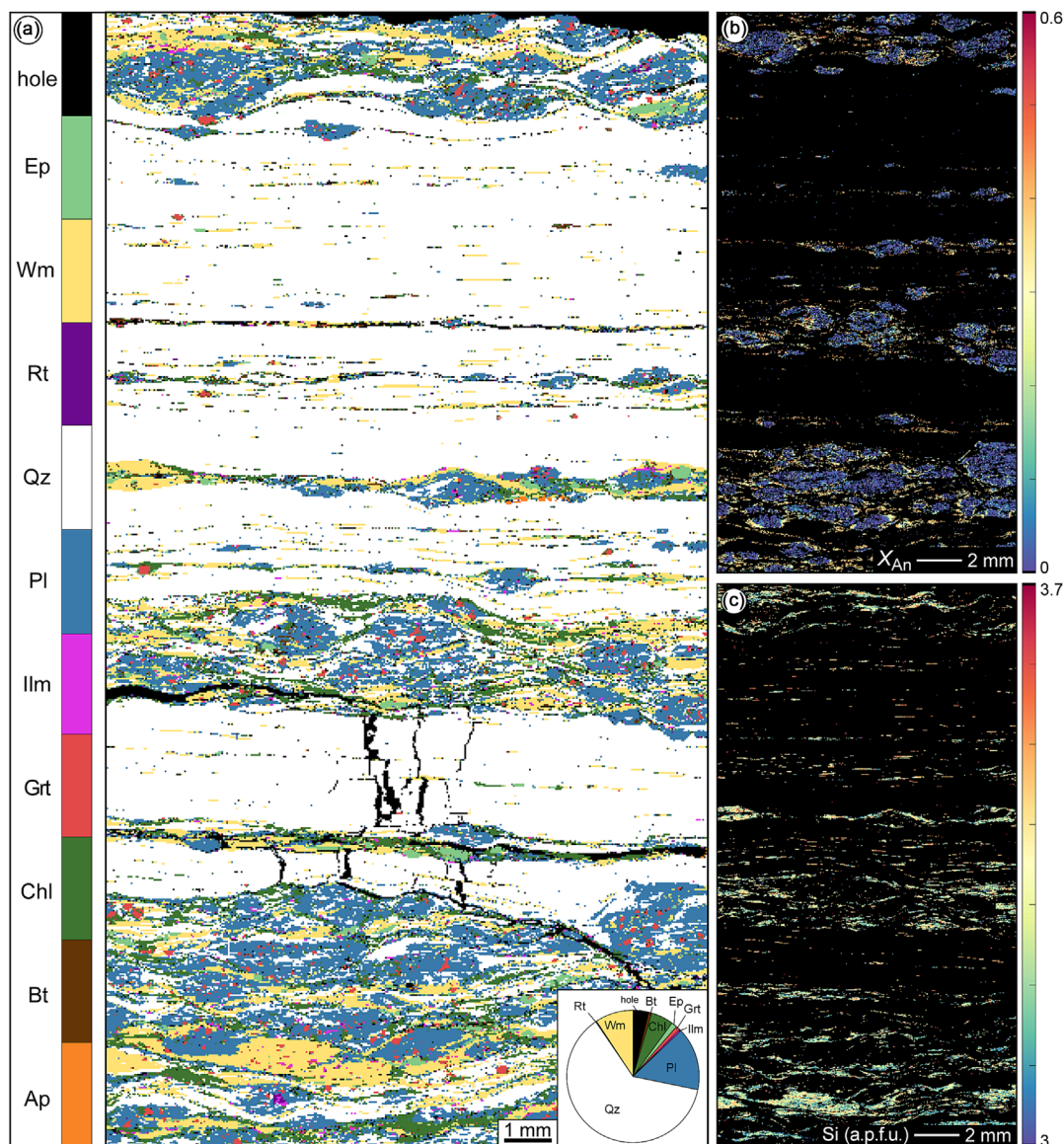


**FIGURE 6** (a) Classified X-ray map of a selected microdomain of sample BAR-8 showing the distribution and abundance of the mineralogical phases; (b)  $X_{An}$  map of plagioclase porphyroblasts, showing oligoclase rims around albite; (c) Si (a.p.f.u.) content map of white mica highlighting its compositional variation with the high-Si content white mica generally in the core of lepidoblasts.

increases to the outer rim from  $X_{Ca} = 0.09$  to  $X_{Ca} = 0.20$ , (ii) a decrease of Mn from core ( $X_{Mn} = 0.05$ – $0.14$ ) to the mantle ( $X_{Mn} = 0.02$ – $0.03$ ) with a slight increase in the rim ( $X_{Mn} = 0.03$ – $0.06$ ), (iii) a decrease of Mg from core ( $X_{Mg} = 0.05$ – $0.07$ ) to mantle ( $X_{Mg} = 0.05$ – $0.06$ ) and a slight increase in the rim, progressively decreasing from  $X_{Mg} = 0.09$  to  $X_{Mg} = 0.03$  and (iv) a roughly flat core and mantle Fe ( $X_{Fe} = 0.60$ – $0.75$ ) content that then shows a sharp increase in the inner rim but progressively decreases from  $X_{Fe} = 0.89$  to  $X_{Fe} = 0.65$ . GrtC and GrtM include chloritoid, with  $X_{Mg} = 0.13$ – $0.14$ , high-Si white mica and rutile (Figure 4e), while GrtR includes biotite (Figure 4f). GrtR is in equilibrium with both albite and

oligoclase (Figure 5b). The chemical variation of garnet, coupled with the presence of different inclusions, highlights a multistage development of garnet porphyroblasts. In sample BAR-8, garnet is quite homogeneous in composition, as no internal zoning can be recognized due to its small size: (i) its Ca content ranges from  $X_{Ca} = 0.07$  to  $X_{Ca} = 0.20$ ; (ii) its Mn content is low ( $X_{Mn} = 0.01$ – $0.07$ ), (iii) its Mg content ranges from  $X_{Mg} = 0.06$  to  $X_{Mg} = 0.15$  and (iv) its Fe content ranges from  $X_{Fe} = 0.65$  to  $X_{Fe} = 0.83$ .

Plagioclase porphyroblasts show a broad pure albite core ( $X_{An} = 0.01$ – $0.04$ ) and a thin oligoclase rim ( $X_{An} = 0.19$ – $0.23$  for sample BAR-4B and  $X_{An} = 0.16$ –



TABLE 1 Representative chemical analyses for sample BAR-4B.

	Garnet			Chloritoid	Plagioclase		White mica		Biotite	Chlorite
	Core	Mantle	Rim		Ab	Pl	Phe	Ms		
SiO <sub>2</sub>	38.00	38.19	37.88	24.77	68.74	62.77	50.94	46.60	36.78	25.74
TiO <sub>2</sub>	0.09	0.06	0.09	0.09	0.00	0.00	0.12	0.03	1.49	0.06
Al <sub>2</sub> O <sub>3</sub>	21.50	21.74	21.48	41.46	20.12	24.20	27.41	34.93	20.45	22.51
Cr <sub>2</sub> O <sub>3</sub>	0.02	0.00	0.00	0.03	0.00	0.00	0.00	0.00	0.09	0.04
FeO <sub>tot</sub>	32.48	32.85	36.48	25.49	0.07	0.11	2.83	2.23	21.52	29.49
MnO	2.92	1.25	1.72	0.13	0.04	0.00	0.01	0.00	0.23	0.21
MgO	1.41	1.12	1.27	2.21	0.00	0.01	2.89	0.74	6.46	11.86
CaO	5.66	7.01	3.95	0.08	0.36	4.94	0.01	0.10	0.08	0.17
Na <sub>2</sub> O	0.10	0.09	0.00	0.01	11.92	9.25	0.30	0.72	0.15	0.03
K <sub>2</sub> O	0.00	0.00	0.01	0.02	0.08	0.09	10.23	8.31	9.32	0.22
Total	102.19	102.31	102.90	94.30	101.34	101.38	94.74	93.66	96.57	90.33
O	12.00	12.00	12.00	14.00	8.00	8.00	11.00	11.00	11.00	28.00
Si	3.00	3.00	2.99	2.01	2.96	2.74	3.42	3.12	2.86	5.40
Ti	0.01	0.00	0.01	0.01	0.00	0.00	0.01	0.00	0.09	0.01
Al	2.00	2.01	2.00	3.97	1.02	1.24	2.17	2.76	1.88	5.56
Cr	0.00	0.00	0.00	0.00	0.00	0.00	0.00	0.00	0.01	0.01
Fe <sup>3+</sup>	0.01	0.00	0.01	0.00	0.00	0.00	0.00	0.00	0.00	0.00
Fe <sup>2+</sup>	2.13	2.16	2.40	1.73	0.00	0.00	0.16	0.13	1.40	5.17
Mn	0.20	0.08	0.12	0.01	0.00	0.00	0.00	0.00	0.01	0.04
Mg	0.17	0.13	0.15	0.27	0.00	0.00	0.29	0.07	0.75	3.71
Ca	0.48	0.59	0.33	0.01	0.02	0.23	0.00	0.01	0.01	0.04
Na	0.02	0.01	0.00	0.00	1.00	0.78	0.04	0.09	0.02	0.01
K	0.00	0.00	0.00	0.00	0.00	0.00	0.88	0.71	0.93	0.06
H	0.00	0.00	0.00	4.00	0.00	0.00	2.00	2.00	2.00	16.00
Σ <sub>cations</sub>	8.00	8.00	8.00	8.00	5.00	5.00	6.95	6.90	7.96	20.00
X <sub>Mg</sub> (Fe <sup>2+</sup> )				0.13			0.65	0.37	0.35	0.42
X <sub>Mg</sub>	0.06	0.04	0.05							
X <sub>Ca</sub>	0.16	0.20	0.11							
X <sub>Mn</sub>	0.07	0.03	0.04							
X <sub>Fe</sub>	0.71	0.73	0.80							
X <sub>An</sub>					0.02	0.23				

0.29 for sample BAR8; Figures 5c and 6b). Albite is mainly characterized by an internal foliation, both discordant (Sp-1, also including garnet; Figure 4a,d) and concordant with the external Sp (Figure 4b). Thus, albite could be interpreted as pre- to syn-tectonic with respect to the main deformational event (Dp). Locally, sheared albite crystals are recognizable. Oligoclase rims are instead developed as strain shadows (Figures 5c and 6b), indicating a syn-tectonic growth with respect to the Sp.

White mica is compositionally variable with Si = 3.08–3.45 a.p.f.u. (atoms per formula unit;

Figure 5d) for BAR-4B and Si = 3.10–3.50 a.p.f.u. for BAR-8 (Figure 6c). A first high-Si content white mica group (Si = 3.25–3.45 a.p.f.u. for BAR-4B and Si = 3.27–3.50 a.p.f.u. for BAR-8) usually defines the Sp-1 in albite and is also present in the core of white mica lepidoblasts along the Sp. A low-Si content white mica group (Si = 3.08–3.13 a.p.f.u. for BAR-4B and Si = 3.10–3.22 a.p.f.u. for BAR-8) overgrows the previous one and defines the Sp together with biotite, chlorite and ilmenite.

Epidote grains found in sample BAR-8 show X<sub>Zo</sub> ranging from 0.44 to 0.59. Biotite is included in the GrtR

TABLE 2 Representative chemical analyses for sample BAR-8.

	Garnet	Epidote	Plagioclase		White mica		Biotite	Chlorite
			Ab	Pl	Phe	Ms		
SiO <sub>2</sub>	38.19	39.08	69.06	62.45	50.53	46.66	37.80	27.98
TiO <sub>2</sub>	0.08	0.15	0.00	0.02	0.45	0.13	1.13	0.04
Al <sub>2</sub> O <sub>3</sub>	22.04	28.14	19.25	23.04	27.47	33.12	18.08	22.45
Cr <sub>2</sub> O <sub>3</sub>	0.00	0.05	0.00	0.04	0.00	0.04	0.00	0.05
FeO <sub>tot</sub>	34.85	7.10	0.08	0.21	2.77	2.61	17.22	28.08
MnO	1.33	0.04	0.00	0.00	0.00	0.01	0.08	0.20
MgO	3.21	0.04	0.02	0.01	2.90	0.99	11.48	9.96
CaO	3.37	23.54	0.10	5.19	0.01	0.02	0.07	0.14
Na <sub>2</sub> O	0.09	0.00	11.51	8.72	0.59	1.25	0.15	0.02
K <sub>2</sub> O	0.01	0.01	0.06	0.09	10.03	9.18	8.73	0.09
Total	103.17	98.15	100.08	99.77	94.75	94.01	94.74	89.01
O	12.00	12.50	8.00	8.00	11.00	11.00	11.00	28.00
Si	2.96	3.01	3.02	2.78	3.39	3.15	2.89	6.00
Ti	0.00	0.01	0.00	0.00	0.02	0.01	0.07	0.01
Al	2.02	2.55	0.99	1.21	2.17	2.64	1.63	5.67
Cr	0.00	0.00	0.00	0.00	0.00	0.00	0.00	0.01
Fe <sup>3+</sup>	0.06	0.46	0.00	0.00	0.00	0.00	0.00	0.00
Fe <sup>2+</sup>	2.20	0.00	0.00	0.01	0.16	0.15	1.10	5.03
Mn	0.09	0.00	0.00	0.00	0.00	0.00	0.01	0.04
Mg	0.37	0.00	0.00	0.00	0.29	0.10	1.31	3.18
Ca	0.28	1.94	0.00	0.25	0.00	0.00	0.01	0.03
Na	0.01	0.00	0.98	0.75	0.08	0.16	0.02	0.01
K	0.00	0.00	0.00	0.00	0.86	0.79	0.85	0.02
H	0.00	1.00	0.00	0.00	2.00	2.00	2.00	16.00
Σ <sub>cations</sub>	8.00	7.98	5.00	5.00	6.97	7.00	7.88	20.00
X <sub>Mg</sub> (Fe <sup>2+</sup> )					0.65	0.40	0.54	0.39
X <sub>Mg</sub>	0.13							
X <sub>Ca</sub>	0.10							
X <sub>Mn</sub>	0.03							
X <sub>Fe</sub>	0.75							
X <sub>An</sub>			0.01	0.25				

of BAR-4B (Figure 4f) and also grows in its strain shadows, defining the Sp. Biotite is also locally recognizable along the main foliation, particularly in BAR-8 (Figure 4h). Few preserved crystals show a relatively homogeneous composition, with  $X_{Mg} = 0.34$ – $0.35$ , in sample BAR-4B, and  $X_{Mg} = 0.46$ – $0.54$ , in sample BAR-8. Chlorite defines the Sp and also grows statically on the Sp, extensively replacing both garnet and biotite (Figure 4h,i). Chlorite displays a composition of  $X_{Mg} = 0.31$ – $0.50$  for sample BAR-4B and  $X_{Mg} = 0.25$ – $0.53$

for sample BAR-8. The rare relict amphibole grains are hornblende, following the classification scheme of Hawthorne et al. (2012).

## 6 | THERMODYNAMIC MODELLING

Thermodynamic forward modelling allows the estimation of the  $P$ – $T$  conditions of rock equilibration by combining

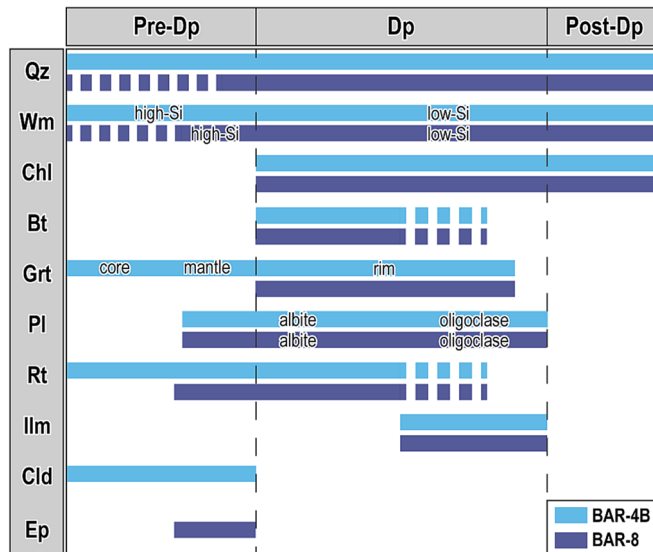


FIGURE 7 Blastesis-deformation relationship diagram of the two analysed samples.

TABLE 3 Bulk compositions of the modelled samples. Bulk I and Bulk II account for garnet core+mantle (GrtC+M) fractionation for sample BAR-4B.

Bulk (wt%)	BAR-4B		BAR-8
	Bulk I	Bulk II	
SiO <sub>2</sub>	55.74	56.70	80.00
TiO <sub>2</sub>	1.00	1.04	0.71
Al <sub>2</sub> O <sub>3</sub>	21.20	21.18	7.90
FeO <sub>tot</sub>	9.45	8.38	2.61
MnO	0.25	0.17	0.06
MgO	2.66	2.71	0.83
CaO	0.52	0.30	0.49
Na <sub>2</sub> O	2.05	2.12	1.50
K <sub>2</sub> O	4.29	4.46	1.29
Total	97.16	97.06	95.38

the mineral composition of one or more coexisting mineral phases. In sample BAR-4B, garnet shows a chemically defined core, mantle and rim. As GrtC and GrtM include only relict phases, the chemical resolution of both garnet and inclusions may not be sufficient to discriminate two events, thus thermodynamic modelling has been conducted grouping GrtC and GrtM, corresponding to the pre-Dp stage. Therefore, calculations with two effective bulk compositions have been performed to account for garnet core+mantle (GrtC+M) fractionation (Bulk I and Bulk II, Table 3). For sample

BAR-8, an explorative  $P$ - $X$  (Fe<sub>2</sub>O<sub>3</sub>) phase diagram at fixed  $T$  has been calculated (Figure S3) to test if epidote needs to be included in the bulk rock composition. The obtained phase diagram predicts amphibole in the whole  $P$  range, whereas BAR-8 only shows a few relicts. Additionally, white mica is predicted only at about  $P > 0.9$  GPa. This is not in agreement with the petrographic observation. Epidote is nevertheless predicted at  $P > 1.0$  GPa. Therefore, in the bulk composition (Table 3) used for  $P$ - $T$  estimations of BAR-8, epidote has been fractionated.

## 6.1 | $P$ - $T$ estimates

Despite the difference in the bulk rock compositions (i.e., two investigated samples, i.e., BAR-4B and BAR-8, and fractionation for BAR-4B), the calculated  $P$ - $T$  isochemical phase diagrams (Figures 8 and 9) show very similar topologies, dominated by three- and four-variant fields, with minor two- and five-variant fields. Elongated narrow fields at 1–1.2 GPa mark the boundary between stable chloritoid and amphibole at higher pressures and albite and chlorite at lower pressures. At ~550–600°C for  $P < 1.3$  GPa, the staurolite-*in* reaction is predicted, mainly consuming chlorite, whereas, at higher pressure, kyanite replaces chloritoid. Garnet is stable in most of the  $P$ - $T$  space in all phase diagrams, but its phase-*in* curve shifts toward higher temperatures in the fractionated phase diagrams of sample BAR-4B. The biotite-*in* reaction is both  $T$ - and  $P$ -dependent, but no biotite can be found stable at  $P > 1.4$  GPa. Rutile is the main stable accessory Ti-phase, which is substituted by ilmenite only at  $T > 480$ °C and  $P < 0.7$ –0.8 GPa.

For sample BAR-4B, calculations with Bulk I show that the association of garnet core+mantle, chloritoid, high-Si white mica and rutile is stable at HP conditions. Glaucofane is predicted at these conditions, whereas only a few re-equilibrated grains of hornblende have been found. Compositional isopleths, corresponding to the measured composition of GrtC+M ( $X_{Mg}$ ,  $X_{Ca}$ ,  $X_{Fe}$ ) coupled with  $X_{Mg}$  of chloritoid and Si a.p.f.u. of white mica, have been used to constrain the first set of  $P$ - $T$  conditions (i.e., pre-Dp; Figure 8a). Considering the maximum overlap among the isopleths used, the first recognized stage (pre-Dp) of BAR-4B evolution can be narrowed at 500–520°C and 1.8–2.2 GPa (Figure 8b).

For sample BAR-4B, calculations with Bulk II show garnet rim associated with the development of the Sp, being in equilibrium with low-Si content white mica, chlorite, biotite and rutile/ilmenite. As previously described, GrtR is in equilibrium with plagioclase, from pure albite to oligoclase (Supplementary Information S1,



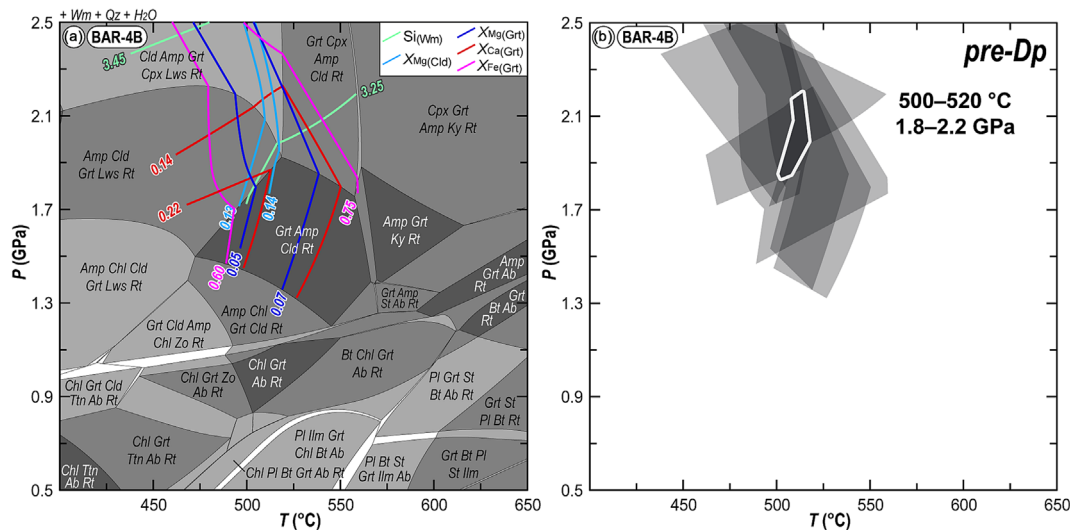


**FIGURE 8** (a)  $P$ - $T$  isochemical phase diagram calculated with Bulk I of sample BAR-4B, where  $X_{Mg}$ ,  $X_{Ca}$  and  $X_{Fe}$  of GrtC+GrtM,  $X_{Mg}$  of chloritoid and Si a.p.f.u. in white mica have been plotted; (b) overlap of the used compositional isopleths, which maximum is highlighted by the white polyline (pre-Dp stage).

Figure 7). The considered compositional isopleths are then  $X_{Mg}$ ,  $X_{Ca}$ ,  $X_{Fe}$ ,  $X_{Mn}$  of GrtR, Si a.p.f.u. of white mica,  $X_{Mg}$  of biotite,  $X_{Mg}$  of chlorite and  $X_{An}$  of plagioclase (Figure 9a). When overlapping the mineral compositional ranges, the Dp stage can be constrained at 520–560 °C, 0.6–0.9 GPa (Figure 9b). The evolution of the chemical zoning of GrtR (i.e., increasing Ca and Mn and decreasing Fe and Mg), the progressive increase in Ca content in plagioclase and biotite chloritization are in agreement with the development of the Dp during decreasing  $T$  and  $P$  (Figure 9b). The albite predicted in the oligoclase field is within model uncertainties.

Sample BAR-8 shows similar phase relation evidence to BAR-4B, with, however, only one recorded growth stage of garnet, which is rather homogeneous and with a composition comparable to that of the GrtR in sample BAR-4B. Garnet growth has been associated with the development of the Sp, being in equilibrium with both low-Si content white mica, chlorite, biotite and rutile/ilmenite. As GrtR of BAR-4B, garnet in BAR-8 is in equilibrium with plagioclase, from pure albite to oligoclase (Supplementary Information S1, Figure 7). The plotted compositional isopleths are  $X_{Mg}$ ,  $X_{Ca}$ ,  $X_{Fe}$ ,  $X_{Mn}$  of garnet, Si a.p.f.u. of low-Si white mica,  $X_{Mg}$  of biotite,  $X_{Mg}$  of chlorite and  $X_{An}$  of plagioclase (Figure 9c). When overlapping the mineral compositional ranges, the Dp stage can be constrained at 530–590 °C, 0.8–1.0 GPa (Figure 9d). The progressive increase in Ca content in plagioclase, together with chlorite substituting biotite, is in agreement with the development of the Dp during decreasing  $T$  and  $P$  (Figure 9d).

## 6.2 | H<sub>2</sub>O content

Since shear zones are major fluid pathways within orogenic wedges,  $P/T$ - $MH_2O$  phase diagrams have been calculated to investigate the influence of H<sub>2</sub>O content variation on the stability of the different stages of the studied samples. Due to the recognized multistage metamorphic history of sample BAR-4B, two  $P/T$ - $MH_2O$  phase diagrams have been calculated along two different  $P$ - $T$  paths using Bulk II (a-a' and b'-b' segments in Figure 10a; see Table S4 for  $P$ - $T$  path equations). This has been done for consistency with previously calculated geobarometric data and to be able to use measured mineral compositions to constrain the amount of H<sub>2</sub>O present in the system during rock re-equilibration. Similarly, for sample BAR-8, two  $P/T$ - $MH_2O$  phase diagrams have been calculated along two different  $P$ - $T$  paths (c-c' and b-b'' segments in Figure 10a; see Table S4 for  $P$ - $T$  path equations). Given (i) the proximity in the field of the two samples and (ii) the similarities in the latest  $P$ - $T$  conditions of rock equilibrations (i.e., Dp stage for both samples), the  $P$ - $T$  path descending from HP conditions for BAR-8 is hinged in the pre-Dp stage of sample BAR-4B. It has been evaluated only below 1.5 GPa. The considered compositional isopleths are the same used to define each growth stage in Figures 8 and 9.

For sample BAR-4B, along the entire decompressive path, the fluid saturation surface shows a complex shape, with both decreasing and increasing H<sub>2</sub>O content. During decompression with an increase in temperature from the pre-Dp stage to the Dp stage (Figure 10b), H<sub>2</sub>O saturation

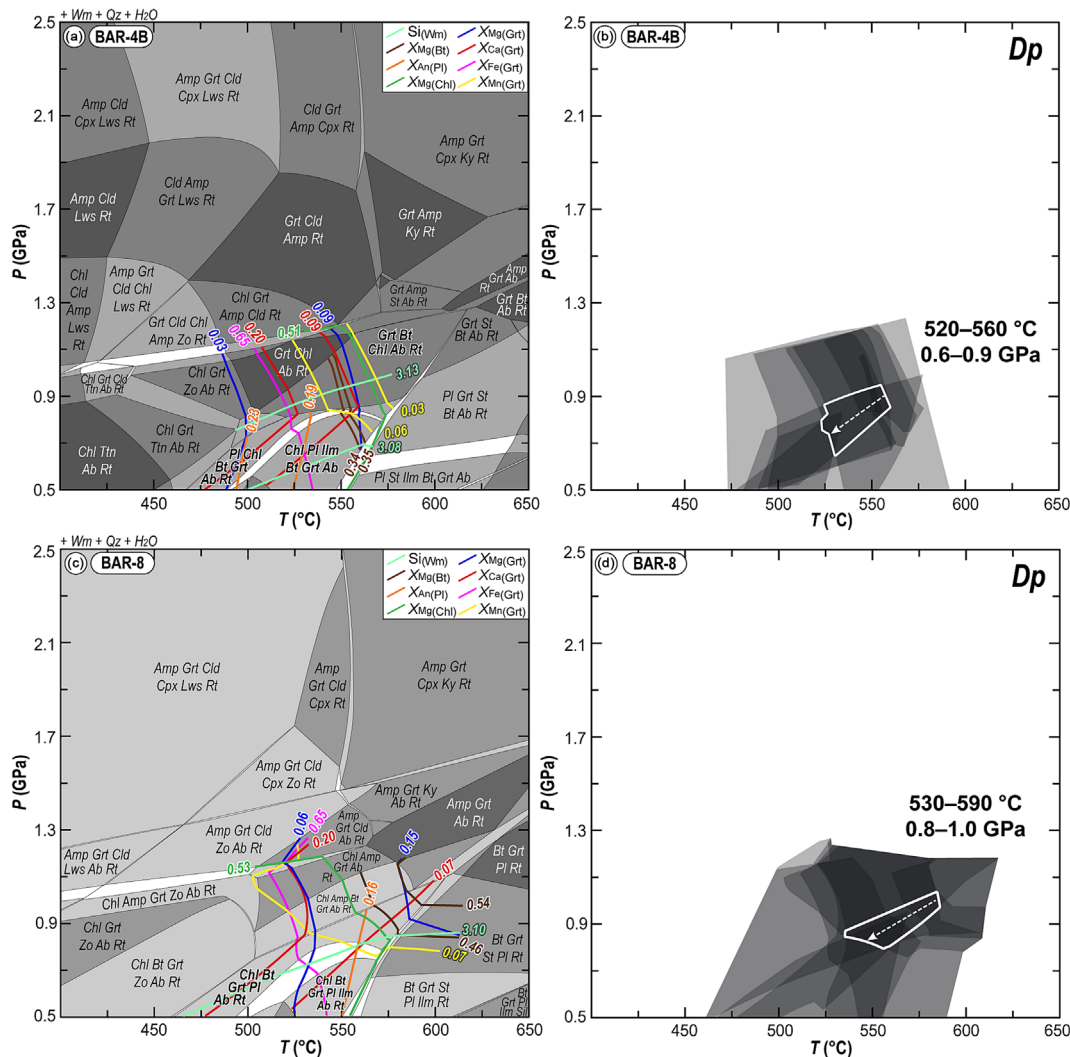


**FIGURE 9** (a)  $P$ - $T$  isochemical phase diagram calculated with Bulk II of sample BAR-4B, where  $X_{Mg}$ ,  $X_{Ca}$ ,  $X_{Fe}$  and  $X_{Mn}$  of GrtR,  $X_{Mg}$  of biotite,  $X_{An}$  of plagioclase,  $X_{Mg}$  of chlorite and Si a.p.f.u. in white mica have been plotted; (b) overlap of the used compositional isopleths, which maximum is highlighted by the white polylines (Dp stage); (c)  $P$ - $T$  isochemical phase diagram calculated for sample BAR-8, where  $X_{Mg}$ ,  $X_{Ca}$ ,  $X_{Fe}$  and  $X_{Mn}$  of garnet,  $X_{Mg}$  of biotite,  $X_{An}$  of plagioclase,  $X_{Mg}$  of chlorite and Si a.p.f.u. in white mica have been plotted; (d) overlap of the used compositional isopleths, which maximum is highlighted by the white polyline (Dp stage).

first decreases from  $\sim 3.25$  wt% reaching a minimum of  $\sim 3.00$  wt% at  $\sim 540^\circ\text{C}$  and 1.2 GPa. Progressively, chlorite and albite start to form and substitute amphibole and chloritoid, suddenly shifting the  $\text{H}_2\text{O}$  saturation value upward, reaching a maximum of  $\sim 3.50$  wt% (i.e., a  $\sim 0.50$  wt% increase) at  $\sim 545^\circ\text{C}$  and 1.1 GPa (Figure 10b). In correspondence with the  $P$ - $T$  conditions of the upper end of the Dp stage, garnet, biotite, white mica and chlorite compositions constrain fluid-saturated conditions for the system. However, when looking at the same compositional space through a different  $P$ - $T$  path (i.e., within the Dp stage, Figure 10c),  $\text{H}_2\text{O}$  undersaturation conditions are required. The lower end of the Dp stage is in a phase field composed of  $\text{Qz} + \text{Grt} + \text{Wm}$

+  $\text{Chl} + \text{Bt} + \text{Pl} + \text{Ilm} + \text{Ab}$  confirming that the stage encompasses both rutile + ilmenite and ilmenite only fields plus the plagioclase-in reaction. This reproduces the dominance of ilmenite along the Sp and the late growth of oligoclase rims. Such conditions occur at  $\sim 520$ - $530^\circ\text{C}$  and  $\sim 0.7$ - $0.8$  GPa and at clearly  $\text{H}_2\text{O}$ -undersaturated conditions, down to  $\sim 3.25$  wt% ( $P/T$ - $\text{MH}_2\text{O}$  highlighted by the dashed yellow arrow in Figure 10c). At these  $P$ - $T$  conditions, the fluid saturation boundary requires  $>3.5$  wt%  $\text{H}_2\text{O}$ .

Regarding sample BAR-8, the fluid saturation surface in the investigated  $P$ - $T$  range starts at  $\sim 0.90$  wt% at  $\sim 540^\circ\text{C}$ , 1.5 GPa. From here, the progressive destabilization of chloritoid and zoisite results in a lowering of the

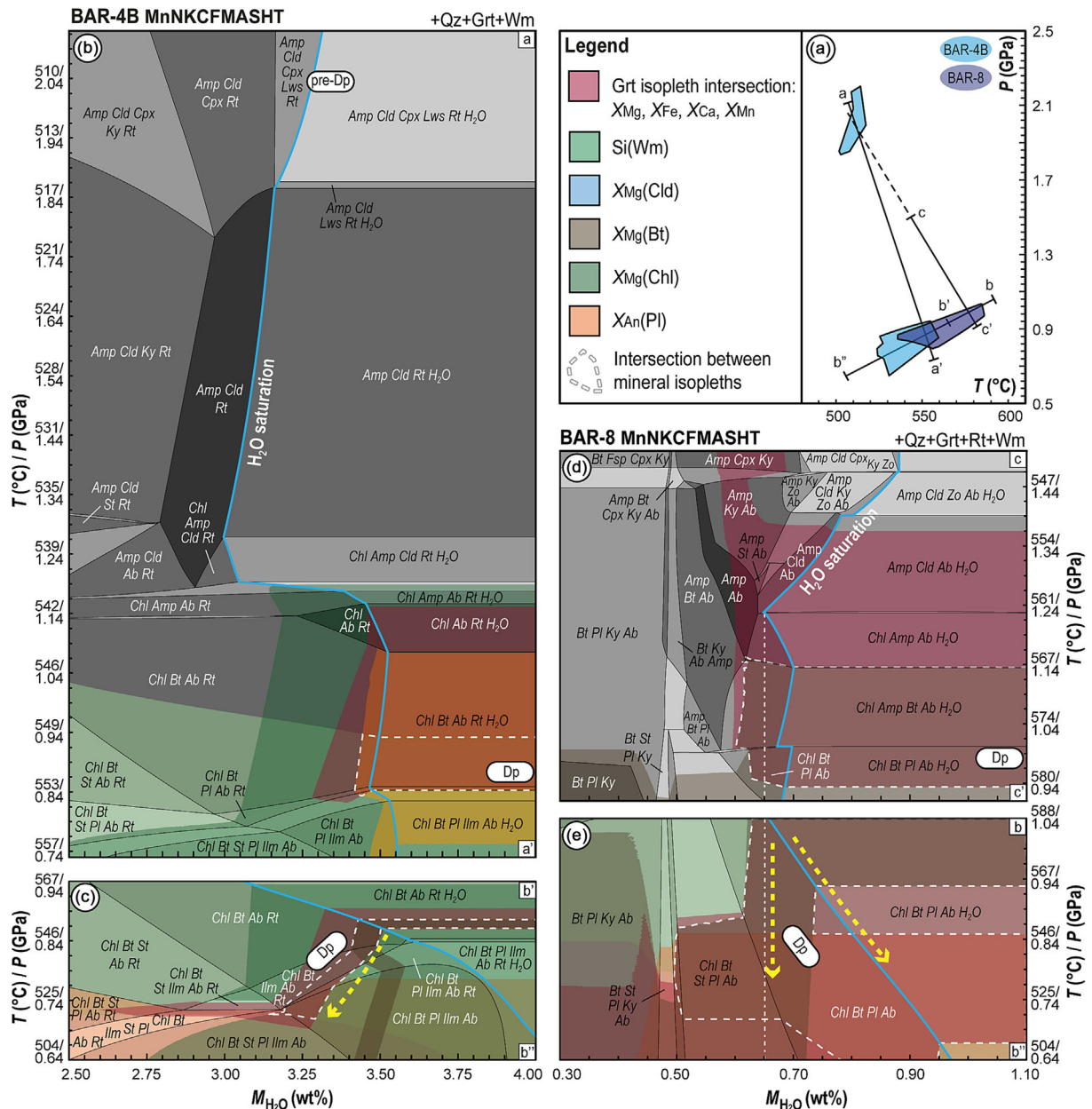


**FIGURE 10** (a)  $P$ - $T$  diagram showing the  $P/T$  gradient segments used to calculate the  $P/T$ - $MH_2O$  phase diagrams; (b-e)  $P/T$ - $MH_2O$  phase diagrams where the thick light blue line represents the  $H_2O$  saturation surface, whereas the coloured fields represent the compositional range of the phases (see Figures 8 and 9). Changing  $MH_2O$  means changing the bulk  $H_2O$  content in the rock. For garnet, the intersection between all its compositional isopleths has directly been reported. The final intersection among all the mineral isopleths is highlighted by the white dashed lines. The isopleth intersections in (d) and (e) allow for both saturated and undersaturated  $H_2O$  conditions.

$H_2O$  saturation surface that reaches a minimum of 0.65 wt% at  $\sim 560^{\circ}C$ -1.2 GPa (Figure 10d). Then, the fluid saturation surface requires a slight increase in the system  $H_2O$  necessary for the stabilization of chlorite and biotite (up to 0.70 wt%, Figure 10d). However, the mineral compositions of the Dp stage define a large  $P/T$ - $MH_2O$  field (marked by a dashed and dotted vertical white line; Figure 10d,e) that allows for  $H_2O$  to both remain at the

minimum of 0.65 wt% which was reached at  $\sim 560^{\circ}C$ -1.20 GPa or at saturation (the dashed yellow line highlighting the possible  $P/T$ - $MH_2O$  evolution paths, Figure 10d,e). The first case would not require further  $H_2O$  to be re-added to the rock. The appearance of staurolite at strongly  $H_2O$ -undersaturated conditions marks the lower boundary for the degree of the Dp<sub>b</sub> stage  $H_2O$  undersaturation (i.e.,  $MH_2O > 0.5$  wt%; Figure 10e).



## 7 | DISCUSSION

### 7.1 | *P–T* path and MBSZ evolution

A multidisciplinary approach (meso- and micro-structural analysis, chemical composition of coexisting phases and thermodynamic modelling) on the mylonitic zone separating the SPU from the RU, i.e., the Mt. Bracco Shear Zone (MBSZ; Avigad et al., 2003) was used to reconstruct its *P–T* evolution. The studied mylonitic samples (BAR-4B and BAR-8), both belonging to the SPU, highlight the presence of different *P–T* stages acquired during the tectono-metamorphic evolution of the MBSZ footwall.

The pre-Dp (Figure 11), recorded only in BAR-4B, is only preserved as chloritoid, high-Si white mica and rutile inclusions in the compositionally defined garnet core. The pre-Dp event can be constrained at 500–520°C and 1.8–2.2 GPa. In the southern part of the DMM, close to our investigated area, *P–T* prograde and peak estimations for the SPU were obtained by Groppo et al. (2019) with methodologies analogous to this study, returning values ~500–520°C, 2.0–2.2 GPa (Figure 11). Previous authors constrained the SPU at lower *P–T* peak conditions (Avigad et al., 2003; Chopin et al., 1991), particularly considering the baric estimations, but not using a forward modelling approach (Figure 11). Recent investigations on rutile (Bonnet et al., 2022) returned Zr-in-rutile peak temperatures of  $513 \pm 20^\circ\text{C}$  when assuming a pressure of 2.2 GPa for the same unit. Thus, pre-Dp conditions recorded in our sample are consistent with the SPU peak estimations of Groppo et al. (2019) and Bonnet et al. (2022), placing the peak *P–T* conditions recorded by the MBSZ within eclogite-facies conditions (Figure 11). The pre-Dp event could be linked to the HP event of Bonnet et al. (2022), constrained at  $32.7 \pm 2.2$  My by U–Pb rutile geochronology.

The Dp event, recorded in both samples, corresponds to the development of the mylonitic Sp foliation linked to the MBSZ activity, associated with low-Si content white mica, biotite, chlorite, garnet (GrtR of sample BAR-4B and whole garnet for sample BAR-8), plagioclase and rutile/ilmenite. The Dp has been constrained at 520–560°C, 0.6–0.9 GPa for sample BAR-4B and at 530–590°C, 0.8–1.0 GPa for sample BAR-8 (Figure 9). Since the Sp has been defined as a composite foliation, the progressive chlorite substitution on biotite, together with the blastesis of syn-kinematic oligoclase represents the continuum of the metamorphic evolution of the Dp toward both decreasing pressure and temperature within the MBSZ. The Dp event related to the MBSZ activity can be overall constrained at ~520–590°C, 0.7–1.0 GPa, developing toward decreasing pressure and temperature (Figure 11).

From the pre-Dp to the Dp event, as recorded by sample BAR-4B, a decompressive evolution coupled with an increase in temperature is detectable. In both samples, garnet growth during decompression is supported by the modelled modes (Figures 12 and 13a,b), which particularly increase at the albite-*in* reaction. During the retrograde path associated with the continuum of the Dp stage, garnet modes decrease when modelled at H<sub>2</sub>O-saturated conditions. However, when considering a fixed H<sub>2</sub>O amount (i.e., at H<sub>2</sub>O-undersaturated conditions: 3.22 wt% for BAR-4B, taken at pre-Dp *P–T* conditions and the minimum H<sub>2</sub>O reached by BAR-8), the garnet modes remain constant (dashed pink line in Figure 12). The Dp *P–T* conditions show several similarities with the retrogressive stage recognized by different authors in the whole DMM, at 500–550°C and ~0.5 GPa (i.e., at amphibolite-facies conditions; Borghi et al., 1985; Sandrone & Borghi, 1992). More specifically to the Mt. Bracco area, early *P–T* estimates by Chopin et al. (1991) for the SPU near the MBSZ, reported similar pressures but at slightly colder conditions (480–540°C, 0.7–1.1 GPa; Figure 11), while the first results on mylonitic samples near our investigated area come from Avigad et al. (2003), whose retrograde *P–T* estimations can be correlated with our Dp mylonitic event at relatively similar *T* and slightly lower *P* (i.e., ~500–600°C, 0.6–0.7 GPa; Figure 11). The differences in the *P–T* estimations for the mylonitic event with respect to Avigad et al. (2003) may result from several sources, namely (i) regional-scale differences in peak pressure and temperature across MBSZ, (ii) different rocks recording different segments of a common *P–T* path, (iii) differences linked to calculation methods. A discussion of these points is outside the scope of this paper.

The post-Dp event is marked by post-kinematic blastesis of chlorite and white mica, as well as extensive chloritization of biotite and garnet. No *P–T* constraints of this stage were possible due to the lack of chemical variation of chlorite and white mica. However, taking into account our retrogressive *P–T* path, we can correlate the post-Dp event to the dominant greenschist-facies ductile fabric observed in the same unit by Chopin et al. (1991).

As summarized in Figure 11, the polyphase *P–T* evolution of the investigated mylonites coming from the footwall of the MBSZ (i.e., belonging to the SPU) agrees with Groppo et al. (2019) and Bonnet et al. (2022), coupled with a similar mylonitic event of Avigad et al. (2003). The mylonitic foliation Sp, parallel to the tectonic unit boundary (MBSZ), started to develop at amphibolite-facies conditions and subsequently continued to evolve under decreasing pressure and temperature.

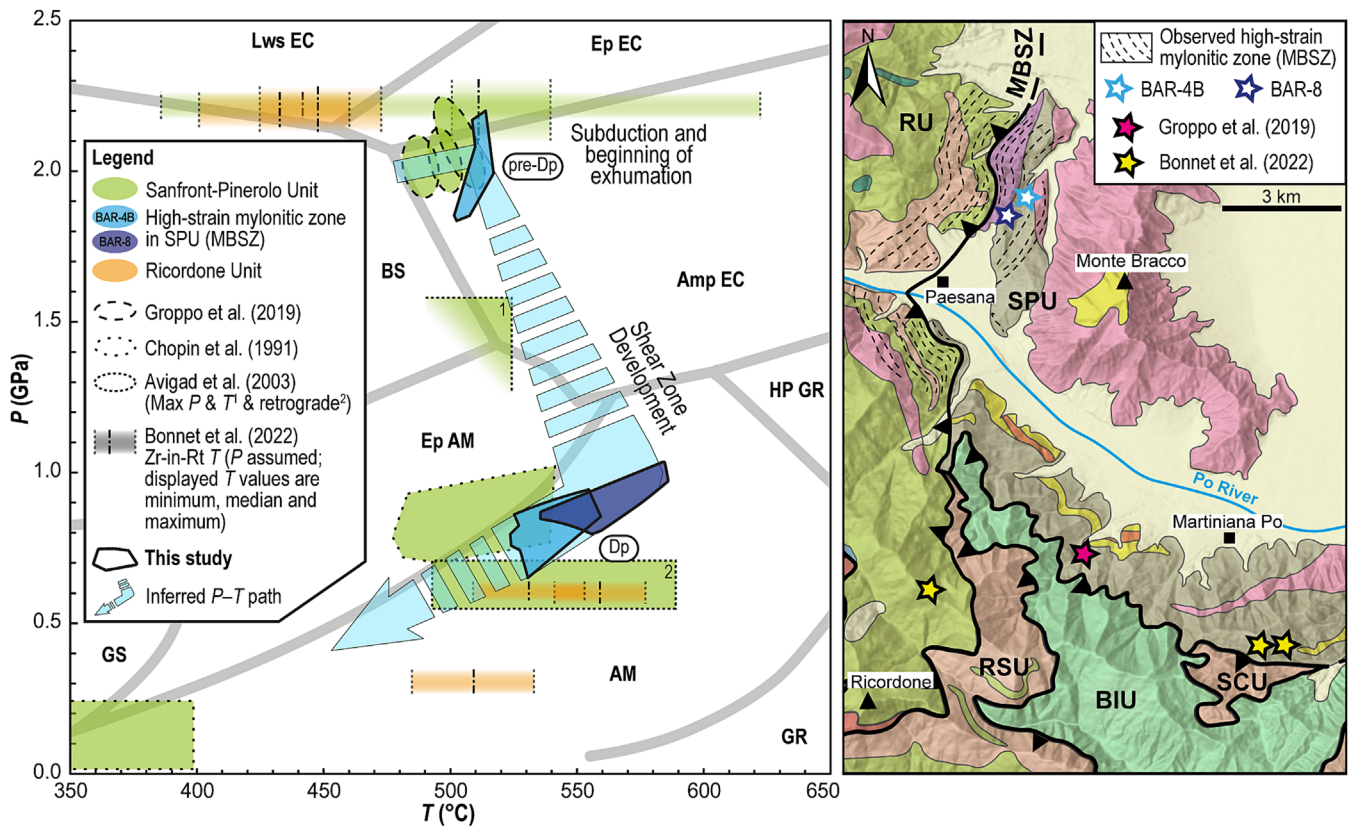


**FIGURE 11** Comparison among literature  $P$ - $T$  conditions estimated for the SPU and the RU and our inferred  $P$ - $T$  for the MBSZ combining the two investigated samples on the left side. Cut-out of Figure 1b (see the legend in the original image) on the right side, where the known position of the samples used by previous authors to reconstruct the metamorphic evolution on the units of our interest is reported. Lws EC: lawsonite eclogite-facies; Ep EC: epidote eclogite-facies; BS: blueschist-facies; Amp EC: amphibole eclogite-facies; Ep AM: epidote amphibolite-facies; HP GR: high-pressure granulite-facies; GS: greenschist-facies; AM: amphibolite-facies; GR: granulite-facies; facies limits are after Liou and Zhang (2002).

## 7.2 | H<sub>2</sub>O evolution along the MBSZ $P$ - $T$ path

Our study also highlights a complex succession of H<sub>2</sub>O loss and gain during the retrograde path and shear zone development and evolution, allowing us to model the dynamic fluid regime that could have affected the MBSZ.

In sample BAR-4B, between the pre-Dp and the Dp stages, thermodynamic modelling predicts a protracted, but limited, initial fluid loss during the transition from eclogite-facies to amphibolite-facies conditions, which then is followed by relevant fluid gain at  $\sim 540^\circ\text{C}$  and  $\sim 1.2$  GPa (Figure 10b). During the protracted fluid loss, the only significant dehydration reaction encountered by the system is the lawsonite breakdown, after which chloritoid progressively destabilizes over a wide  $P$ - $T$  range. The position of the H<sub>2</sub>O saturation surface reaches, at its minimum, an H<sub>2</sub>O content that is even lower than what is reached at the metamorphic peak (pre-Dp stage).

Assuming H<sub>2</sub>O-saturated conditions, chlorite becomes stable in the mineral assemblage at  $\sim 540^\circ\text{C}$ , 1.2 GPa. At slightly lower pressure, thermodynamic modelling predicts the final amphibole and chloritoid breakdown, leading to strong production of albite, chlorite and minor garnet (Figure 13a), requiring an increase of at least  $\sim 0.50$  wt% of H<sub>2</sub>O. Assuming that H<sub>2</sub>O saturation conditions have been maintained during the eclogite- to amphibolite-facies transition, phyllosilicates increase from  $\sim 39$  vol% to  $\sim 54$  vol% (Figure 13a). Indeed, the strong re-equilibration of the mineral assemblage and obliteration of most, if not all, prograde to peak evidence proves that fluid-present conditions were attained. The chlorite compositional range (see the dark-green field in Figure 10b) supports that the bulk of the observed chlorite crystals formed during this H<sub>2</sub>O ingress into the system.

At the same time, BAR-8 experiences a more pronounced H<sub>2</sub>O loss due to the destabilization of zoisite, amphibole and chloritoid, with the latter being

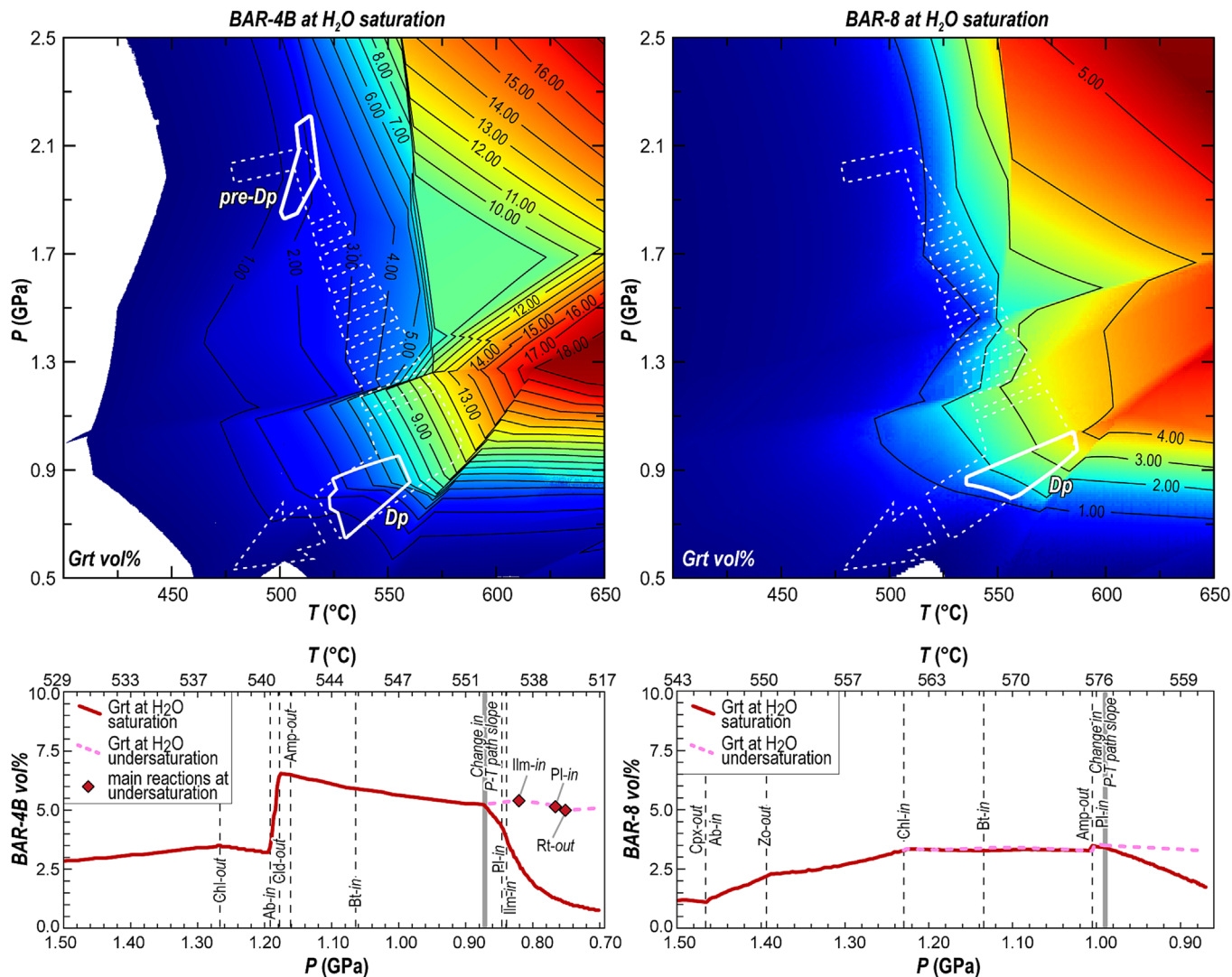


**FIGURE 12** Modal variation of garnet in the  $P$ - $T$  space calculated at  $H_2O$ -saturated conditions for both BAR-4B and BAR-8 samples at the top. At  $\sim 1.2$  GPa, garnet modes abruptly increase. In the lower part, garnet modes were calculated along the  $P/T$  paths of the two samples at saturated and undersaturated  $H_2O$  conditions for both BAR-4B and BAR-8 samples. At  $H_2O$ -saturated conditions, garnet modes increase from the pre-Dp to the Dp stage and decrease during the Dp evolution towards decreasing  $P$  and  $T$ . When modelling at fixed (undersaturated)  $H_2O$  content, garnet vol% (dashed pink line) remains constant from higher to lower pressure and temperature.

substituted by chlorite at  $\sim 560^\circ\text{C}$ , 1.2 GPa (Figures 10d and 13b). At these conditions, the  $H_2O$  content of the system reaches a minimum. The compositional isopleths for the Dp stage allow for both saturated and undersaturated  $H_2O$  conditions. The already low proportion of phyllosilicates (11 vol%) is only marginally increased during exhumation from eclogite-facies to amphibolite-facies conditions (Figure 13b). Noticeably, the modelled modes of all phases are consistent for both  $H_2O$ -saturated and -undersaturated conditions (Figure 13b).

Overall, as shown in Figure 14, the  $H_2O$  content evolution of samples BAR-4B and BAR-8 shows a similar decrease, with both reaching their  $H_2O$  minimum at

the eclogite- to amphibolite-facies transition. However, as BAR-4B requires (at  $\sim 1.2$ – $1.3$  GPa) relevant  $H_2O$  addition, BAR-8 (at  $\sim 1.2$  GPa) does not require further  $H_2O$  addition to stabilize the observed mineralogy and their composition. In fact, according to experiments, the minimum amount of  $H_2O$  necessary to qualify a system as “hydrous” is very low (Milke et al., 2013). Thus, even a small increase in  $H_2O$  is sufficient to trigger metamorphic reactions under geologically realistic timescales. Additionally, with constant confining pressure an increasing  $H_2O$  content causes a decrease in the material strength (Griggs, 1967; Gueydan et al., 2014), possibly determining the shear zone development. Due to



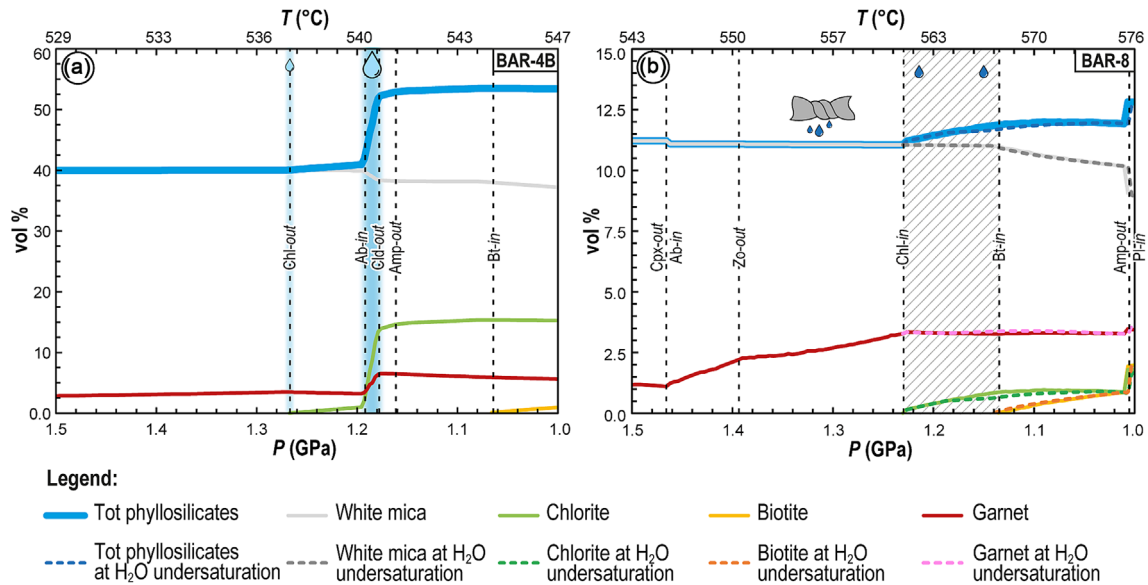


**FIGURE 13** Modal variation of phases along the retrograde  $P$ - $T$  path from 1.5 GPa down to 1 GPa for (a) BAR-4B and (b) BAR-8. Solid lines are calculated along the H<sub>2</sub>O saturation surface, while the dashed lines in (b) are calculated at undersaturated and fixed H<sub>2</sub>O content along the dashed and dotted straight line in Figure 10d,e. Dashed black lines are reactions while the shaded light blue fields in (a) and the striped field in (b) represent an addition of H<sub>2</sub>O to the system, as shown in Figure 14.

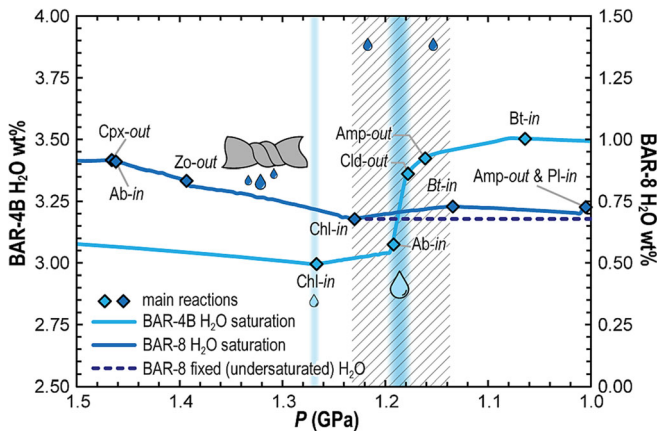


**FIGURE 14** Change in H<sub>2</sub>O amount modelled at saturation (solid lines), along the same retrograde  $P$ - $T$  paths of Figure 13, in both BAR-4B and BAR-8 samples. The fixed (undersaturated) H<sub>2</sub>O content for BAR-8 is taken from Figure 10d,e. The main reactions that modify the H<sub>2</sub>O content in the system are reported.

the spatial proximities of the samples, it can be postulated that at least part of the H<sub>2</sub>O required by lithotypes like BAR-4B, in addition to possible external fluid (relative to the developing shear zone as a whole), might be in part internally derived by other portions of the shear zone constituted by BAR-8-like lithotypes (Figure 15).

Continuing along the exhumation path, during the Dp stage the drastic change in the exhumation  $P$ - $T$  path

and its record in the mineral compositions leads to the attainment of strongly H<sub>2</sub>O-undersaturated conditions in both samples (Figure 10). Such change in H<sub>2</sub>O behaviour does not lead to changes in the estimated  $P$ - $T$  conditions of rock equilibration derived from classical  $P$ - $T$  isochemical phase diagrams (Figures 8 and 9). However, it suggests that the MBSZ evolved during cooling in an H<sub>2</sub>O-undersaturated closed system. The kinetics of metamorphic reactions under these conditions are expected to be very slow, limiting the reaction product formation (Proyer, 2003; Ceccato et al., 2020; Nerone et al., 2023). Thus, this can explain the incomplete re-equilibration observed across the Dp stage, despite intensive deformation.

Finally, after having shown how sample BAR-4B records a complex history of fluid loss and gain, starting from H<sub>2</sub>O saturation conditions, followed by late H<sub>2</sub>O-undersaturated conditions, we demonstrated that the final H<sub>2</sub>O content is higher than at the eclogitic metamorphic peak. However, thermodynamic modelling studies commonly consider rocks undergoing only fluid loss during increasing temperature, which would hamper retrograde reactions and preserve the prograde assemblage (Rubie, 1986; Tenczer et al., 2006). This implies that the H<sub>2</sub>O content modelled at peak  $P$ - $T$  conditions would not change during cooling (e.g., Guiraud et al., 2001; Manzotti et al., 2022). Thus, one common modelling assumption is to keep the H<sub>2</sub>O left at the metamorphic peak in the bulk rock composition and use that fixed



value to model retrograde phase relations (e.g., Guiraud et al., 2001; Manzotti et al., 2022). To test this scenario, we calculated an additional isochemical phase diagram for BAR-4B with Bulk II and the peak H<sub>2</sub>O content of 3.13 wt%. For this specific case study, however, this resulted in a petrologic model that is less consistent with the observed mineralogical assemblage and the corresponding mineral compositions (Figure S4). In particular, the Dp stage would fall in the H<sub>2</sub>O-undersaturated part of the diagram. Consequently, staurolite is predicted to be stable in a wider *P*–*T* space, affecting the biotite compositional range, which is at conditions not consistent with the observed assemblage. The compositional range of plagioclase also falls in the staurolite stability field, whereas no staurolite has been recognized in our samples. For these reasons, in the case of the MBSZ, keeping a fixed H<sub>2</sub>O content does not allow for a reliable reconstruction of the MBSZ *P*–*T* path.

### 7.3 | Implication for fluid circulation in shear zones

Fluids in the Earth's crust move preferentially through shear zones and commonly promote deformation inducing a grain size reduction, which, in turn, further

facilitates mineral reactions (Beach, 1980; Brodie & Rutter, 1987; De Bresser et al., 2001; Fyfe et al., 1978; Getsinger et al., 2013; Jamtveit et al., 2008; Menegon et al., 2015). For this reason, shear zones have been generally regarded to be evolving at H<sub>2</sub>O-saturated conditions (e.g., Etheridge et al., 1983; Guiraud et al., 2001; McCaig et al., 1990; Rubie, 1986; Tursi et al., 2018). However, transient fluid regimes from H<sub>2</sub>O-undersaturated to H<sub>2</sub>O-saturated conditions have also been observed (e.g., Ceccato et al., 2020; Diener et al., 2016; Tursi, 2022). Ductile shear zones may be enhanced by fluid presence but also may redistribute fluid, allowing the attainment of transient conditions thanks to deformation-driven fluid channelling (e.g., Ceccato et al., 2020, 2021; Connolly, 1997; Nerone et al., 2023; Thompson, 1983; Tursi et al., 2021; Tursi, 2022). The overall evolution of the MBSZ is, in fact, affected by such changing conditions (Figure 15). The investigated samples highlight how the preservation of HP relicts can be different in function of their involvement within the shear zone and ultimately in their H<sub>2</sub>O evolution. The H<sub>2</sub>O behaviour of the two samples can be directly linked to the different protolith, which ultimately controls the availability of hydrate phases. Due to these considerations, when reconstructing the metamorphic evolution of ductile shear zones, assessing the H<sub>2</sub>O content in the studied samples might be helpful when using thermodynamic modelling in order to validate the chosen assumptions (i.e., fluid-absent conditions during the retrograde *P*–*T* path vs. fluid saturation during the overall *P*–*T* evolution). As such, the MBSZ well displays how fluid content variations may be complex within shear zones (Figure 15).

## 8 | CONCLUSIONS

In this work, our microstructural, chemical and forward thermodynamic modelling study supports the following conclusions:

- The MBSZ, located at the boundary between HP units of the Dora Maira Massif in the Western Alps, separating the polymetamorphic and the monometamorphic complexes, displays a polyphase evolution. It records relict eclogite-facies conditions and a main composite mylonitic event during exhumation at amphibolite-facies conditions;
- The *P*/*T*–*MH*<sub>2</sub>O forward modelling highlights different behaviour for the two analysed samples. After reaching a minimum in the H<sub>2</sub>O content at the transition from eclogite- to amphibolite-facies conditions, a significant fluid gain is predicted for only one

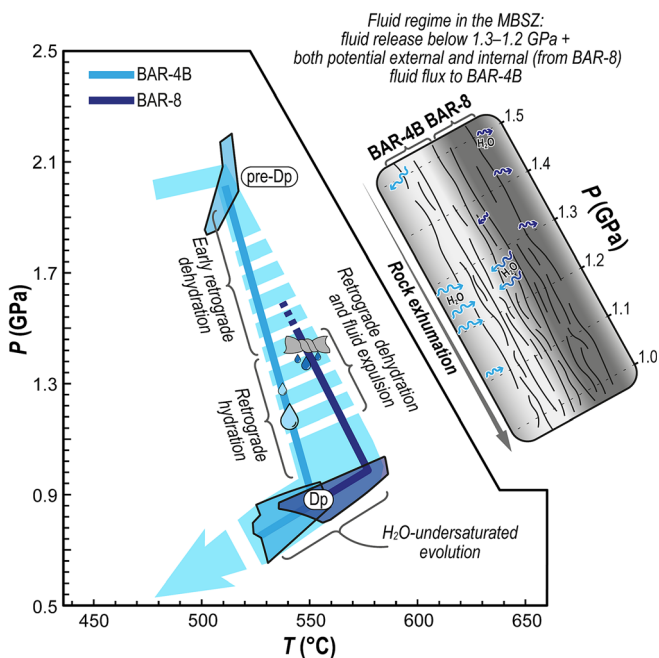


**FIGURE 15** Conceptual model of the *P*–*T* evolution and the associated fluid regimes that aided the development of the MBSZ during exhumation from eclogite- to amphibolite-facies conditions. A small sketch displaying the internally and externally derived H<sub>2</sub>O budget along the first exhumation path is provided.

sample, just before the mylonitic event, while the other experiences fluid loss. During the further evolution toward lower  $P$ - $T$  conditions, the MBSZ evolves under  $H_2O$ -undersaturated conditions in a closed system;

- This difference in behaviour suggests that the fluid evolution within shear zones could result from both externally and internally derived fluid flux and that different fluid circulation regimes may be present in different portions of a shear zone.

Overall, a complex evolution of gain and loss of fluid within the MBSZ better explains the observed microstructures and mineral composition, highlighting how assuming a fixed  $H_2O$  content for shear zones can result in mismatches between observations and models. It is therefore best practice to test for each case study, which is the best modelling approach that will lead to the best reproduction of the natural evidence.

## ACKNOWLEDGMENTS

We are thankful to S. Schorn and M. Ballèvre for their thorough reviews which significantly improved the initial version of the manuscript and to B. Cesare for editorial handling.

## CONFLICT OF INTEREST STATEMENT

The authors declare that they have no competing financial interests or personal relationships that could have appeared to influence the work reported in this paper.

## DATA AVAILABILITY STATEMENT

The data that supports the findings of this study are available in the manuscript and in the supplementary material of this article.

## ORCID

Sara Nerone  <https://orcid.org/0000-0001-7277-2454>

Alessandro Petroccia  <https://orcid.org/0000-0001-5230-0046>

Fabiola Caso  <https://orcid.org/0000-0002-1136-2811>

Davide Dana  <https://orcid.org/0000-0002-3296-2365>

Andrea Maffei  <https://orcid.org/0000-0001-9179-1730>

## REFERENCES

- Angrand, P., & Mouthereau, F. (2021). Evolution of the Alpine orogenic belts in the Western Mediterranean region as resolved by the kinematics of the Europe-Africa diffuse plate boundary. *BSGF-Earth Sciences Bulletin*, 192(1), 42. <https://doi.org/10.1051/bsgf/2021031>
- Argand, E. (1911). Les nappes de recouvrement des Alpes Pennines et leurs prolongements structuraux. In *Matériaux Pour La Carte Géologique De La Suisse* (Vol. 31). Nouvelle Série. (p. 26).
- Argand, E. (1934). La zone pennique. In *Guide Géologique de la Suisse. Introductions Générales* (Vol. 3) (pp. 149–189). Wepf & Co.
- Avigad, D. (1992). Exhumation of coesite-bearing rocks in the Dora Maira massif (western Alps, Italy). *Geology*, 20(10), 947–950. [https://doi.org/10.1130/0091-7613\(1992\)020%3C0947:EOCBRI%3E2.3.CO;2](https://doi.org/10.1130/0091-7613(1992)020%3C0947:EOCBRI%3E2.3.CO;2)
- Avigad, D., Chopin, C., & Le Bayon, R. (2003). Thrusting and extension in the southern Dora-Maira ultra-high-pressure massif (Western Alps): View from below the Coesite-bearing unit. *The Journal of Geology*, 111(1), 57–70. <https://doi.org/10.1086/344664>
- Ballèvre, M., Camonin, A., Manzotti, P., & Poujol, M. (2020). A step towards unraveling the paleogeographic attribution of pre-Mesozoic basement complexes in the Western Alps based on U–Pb geochronology of Permian magmatism. *Swiss Journal of Geosciences*, 113(1), 1–28. <https://doi.org/10.1186/s00015-020-00367-1>
- Beach, A. (1980). Retrogressive metamorphic processes in shear zones with special reference to the Lewisian complex. *Journal of Structural Geology*, 2, 257–263. [https://doi.org/10.1016/0191-8141\(80\)90058-9](https://doi.org/10.1016/0191-8141(80)90058-9)
- Beltrando, M., Compagnoni, R., & Lombardo, B. (2010). (ultra-) high-pressure metamorphism and orogenesis: An Alpine perspective. *Gondwana Research*, 18, 147–166. <https://doi.org/10.1016/j.gr.2010.01.009>
- Bonnet, G., Chopin, C., Locatelli, M., Kylander-Clark, A. R., & Hacker, B. R. (2022). Protracted subduction of the European hyperextended margin revealed by rutile U–Pb geochronology across the Dora-Maira massif (Western Alps). *Tectonics*, 41(4), e2021TC007170. <https://doi.org/10.1029/2021TC007170>
- Borghi, A., Cadoppi, P., Porro, A., & Sacchi, R. (1985). Metamorphism in the northern part of the Dora-Maira massif (Cottian Alps). *Museo Regionale di Scienze Naturali di Torino, Bollettino*, 3, 369–380.
- Borghi, A., Compagnoni, R., & Sandrone, R. (1996). Composite P–T paths in the internal Penninic massifs of the Western Alps: Petrological constraints to their thermo-mechanical evolution. *Ecolgae Geologicae Helveticae*, 89, 345–367. <https://doi.org/10.5169/seals-167905>
- Brodie, K. H., & Rutter, E. H. (1987). The role of transiently fine-grained reaction products in syntectonic metamorphism: Natural and experimental examples. *Canadian Journal of Earth Sciences*, 24(3), 556–564. <https://doi.org/10.1139/e87-054>
- Bussy, F., & Cadoppi, P. (1996). U–Pb zircon dating of granulites from the Dora-Maira massif (western Italian Alps). *Schweizerische Mineralogische Und Petrographische Mitteilungen*, 76, 217–233.
- Carosi, R., Petroccia, A., Iaccarino, S., Simonetti, M., Langone, A., & Montomoli, C. (2020). Kinematics and timing constraints in a transpressive tectonic regime: The example of the posada-Asinara shear zone (NE Sardinia, Italy). *Geosciences*, 10(8), 288. <https://doi.org/10.3390/geosciences10080288>
- Cavallo, A., & Dino, G. A. (2019). The *Bargiolina*, a striking historical stone from Monte Bracco (Piedmont, NW Italy) and a possible source of industrial minerals. *Sustainability*, 11(16), 4293. <https://doi.org/10.3390/su11164293>

- Ceccato, A., Goncalves, P., & Pennacchioni, G. (2020). Temperature, fluid content and rheology of localized ductile shear zones in subsolidus cooling plutons. *Journal of Metamorphic Geology*, 38(8), 881–903. <https://doi.org/10.1111/jmg.12553>
- Ceccato, A., Viola, G., Tartaglia, G., & Antonellini, M. (2021). In-situ quantification of mechanical and permeability properties on outcrop analogues of offshore fractured and weathered crystalline basement: Examples from the Rolvsnes granodiorite, Bømlø, Norway. *Marine and Petroleum Geology*, 124, 104859. <https://doi.org/10.1016/j.marpetgeo.2020.104859>
- Chopin, C., Henry, C., & Michard, A. (1991). Geology and petrology of the coesite-bearing terrain, Dora Maira massif, Western Alps. *European Journal of Mineralogy*, III, 263–291. <https://doi.org/10.1127/ejm/3/2/0263>
- Compagnoni, R., Elter, G., & Lombardo, B. (1974). Eterogeneità stratigrafica del complesso degli “Gneiss Minuti” nel massiccio cristallino del Gran Paradiso. *Memorie Della Societa Geologica Italiana*, 13, 227–239.
- Compagnoni, R., Rolfo, F., Groppo, C., Hirajima, T., & Turello, R. (2012). Geological map of the ultra-high pressure Brossasco-Isasca unit (Western Alps, Italy). *Journal of Maps*, 8(4), 465–472. <https://doi.org/10.1080/17445647.2012.744367>
- Connolly, J. A. D. (1997). Devolatilization-generated fluid pressure and deformation-propagated fluid flow during prograde regional metamorphism. *Journal of Geophysical Research - Solid Earth*, 102(B8), 18149–18173. <https://doi.org/10.1029/97jb00731>
- Connolly, J. A. D. (2005). ComputAtion of phase equilibria by linear programming: a tool for geodynamic modeling and its application to subduction zone decarbonation. *Earth and Planetary Science Letters*, 236(1–2), 524–541. <https://doi.org/10.1016/j.epsl.2005.04.033>
- Connolly, J. A. D. (2009). The geodynamic equation of state: What and how. *Geochemistry, Geophysics, Geosystems*, 10(10), Q10014. <https://doi.org/10.1029/2009GC002540>
- Crema, G., Dal Piaz, G., Merlo, C., & Zanella, E. (1971). Note esplicative della carta geologica d'Italia alla scala 1:100.000 (foglio Argentera - Dronero). *Servizio Geologico d'Italia*. [http://sgi.isprambiente.it/geologia100k/mostra\\_foglio.aspx?numero\\_foglio=78-79#](http://sgi.isprambiente.it/geologia100k/mostra_foglio.aspx?numero_foglio=78-79#)
- De Andrade, V., Vidal, O., & Lewin, E. (2006). Quantification of electron microprobe compositional maps of rock thin sections: An optimized method and examples. *Journal of Metamorphic Geology*, 24(7), 655–668. <https://doi.org/10.1111/j.1525-1314.2006.00660.x>
- De Bresser, J., Ter Heege, J., & Spiers, C. (2001). Grain size reduction by dynamic recrystallization: Can it result in major rheological weakening? *International Journal of Earth Sciences*, 90, 28–45. <https://doi.org/10.1007/S005310000149>
- Diener, J. F. A., Fagereng, Å., & Thomas, S. A. J. (2016). Mid-crustal shear zone development under retrograde conditions: Pressure–temperature–fluid constraints from the Kuckaus Mylonite zone, Namibia. *Solid Earth*, 7(5), 1331–1347. <https://doi.org/10.5194/se-7-1331-2016>
- Dino, G. A., Cavallo, A., Faraudello, A., Rossi, P., & Mancini, S. (2021). Raw materials supply: Kaolin and quartz from ore deposits and recycling activities. The example of the Monte Bracco area (Piedmont, northern Italy). *Resources Policy*, 74, 102413. <https://doi.org/10.1016/j.resourpol.2021.102413>
- Etheridge, M. A., Wall, V. J., & Vernon, R. H. (1983). The role of the fluid phase during regional metamorphism and deformation. *Journal of Metamorphic Geology*, 1(3), 205–226. <https://doi.org/10.1111/j.1525-1314.1983.tb00272.x>
- Ferrando, S., Groppo, C., Frezzotti, M. L., Castelli, D., & Proyer, A. (2017). Dissolving dolomite in a stable UHP mineral assemblage: Evidence from Cal-Dol marbles of the Dora-Maira massif (Italian Western Alps). *American Mineralogist*, 102(1), 42–60. <https://doi.org/10.2138/am-2017-5761>
- Finch, M. A., Weinberg, R. F., & Hunter, N. J. R. (2016). Water loss and the origin of thick ultramylonites. *Geology*, 44(8), 599–602. <https://doi.org/10.1130/G37972.1>
- Forshaw, J. B., & Pattison, D. R. M. (2021). Ferrous/ferric (Fe<sup>2+</sup>/Fe<sup>3+</sup>) partitioning among silicates in metasedimentary rocks. *Contributions to Mineralogy and Petrology*, 176, 63. <https://doi.org/10.1007/s00410-021-01814-4>
- Forshaw, J. B., & Pattison, D. R. M. (2023). Major-element geochemistry of pelites. *Geology*, 51(1), 39–43. <https://doi.org/10.1130/G50542.1>
- Franchi, S., & Novarese, V. (1895). Appunti geologici e petrografici sui dintorni di Pinerolo. *Bollettino del Regio Comitato Geologico d'Italia*, 26, 385–429.
- Fuhrman, M. L., & Lindsley, D. H. (1988). Ternary-feldspar modeling and thermometry. *American Mineralogist*, 73, 201–215.
- Fyfe, W. S., Price, N. J., & Thompson, A. B. (1978). *Fluids in the Earth's crust: Their significance in metamorphic, tectonic, and chemical transport processes* (p. 372). Elsevier.
- Gasco, I., Gattiglio, M., & Borghi, A. (2013). Review of metamorphic and kinematic data from internal crystalline massifs (Western Alps): PTt paths and exhumation history. *Journal of Geodynamics*, 63, 1–19. <https://doi.org/10.1016/j.jog.2012.09.006>
- Gerbi, C., Culshaw, N., & Marsh, J. (2010). Magnitude of weakening during crustal-scale shear zone development. *Journal of Structural Geology*, 32, 107–117. <https://doi.org/10.1016/j.jsg.2009.10.002>
- Getsinger, A. J., Hirth, G., Stünitz, H., & Goergen, E. T. (2013). Influence of water on rheology and strain localization in the lower continental crust. *Geochemistry, Geophysics, Geosystems*, 14, 2247–2264. <https://doi.org/10.1002/ggge.20148>
- Giuntoli, F., Menegon, L., Warren, C. J., Darling, J., & Anderson, M. W. (2020). Protracted shearing at midcrustal conditions during large-scale thrusting in the Scandinavian Caledonides. *Tectonics*, 39(9), e2020TC006267. <https://doi.org/10.1029/2020TC006267>
- Goncalves, P., Olliot, E., Marquer, D., & Connolly, J. A. D. (2012). Role of chemical processes on shear zone formation: An example from the grimsel metagranodiorite (Aar massif, Central Alps). *Journal of Metamorphic Geology*, 30(7), 703–722. <https://doi.org/10.1111/j.1525-1314.2012.00991.x>
- Goncalves, P., Poilvet, J. C., Olliot, E., Trap, P., & Marquer, D. (2016). How does shear zone nucleate? An example from the Suretta nappe (Swiss eastern Alps). *Journal of Structural Geology*, 86, 166–180. <https://doi.org/10.1016/j.jsg.2016.02.015>
- Green, E. C. R., Holland, T. J. B., & Powell, R. (2007). An order-disorder model for omphacitic pyroxenes in the system jadeite-diopside-hedenbergite-acmite, with applications to eclogite rocks. *American Mineralogist*, 92, 1181–1189. <https://doi.org/10.2138/am.2007.2401>



- Green, E. C. R., White, R. W., Diener, J. F. A., Powell, R., Holland, T. J. B., & Palin, R. M. (2016). Activity–composition relations for the calculation of partial melting equilibria in metabasic rocks. *Journal of Metamorphic Geology*, 34(9), 845–869. <https://doi.org/10.1111/jmg.12211>
- Griggs, D. T. (1967). Hydrolytic weakening of quartz and other silicates. *Geophysical Journal of the Royal Astronomical Society*, 14, 19–31. <https://doi.org/10.1111/j.1365-246X.1967.tb06218.x>
- Groppo, C., Ferrando, S., Gilio, M., Botta, S., Nosenzo, F., Balestro, G., Festa, A., & Rolfo, F. (2019). What's in the sandwich? New P–T constraints for the (U)HP nappe stack of southern Dora-Maira massif (Western Alps). *European Journal of Mineralogy*, 31(4), 665–683. <https://doi.org/10.1127/ejm/2019/0031-2860>
- Gueydan, F., Précigout, J., & Montési, L. G. J. (2014). Strain weakening enables continental plate tectonics. *Tectonophysics*, 631, 189–196. <https://doi.org/10.1016/j.tecto.2014.02.005>
- Guiraud, M., Powell, R., & Rebay, G. (2001). H<sub>2</sub>O in metamorphism and unexpected behaviour in the preservation of metamorphic assemblages. *Journal of Metamorphic Geology*, 19, 445–454. <https://doi.org/10.1046/j.0263-4929.2001.00320.x>
- Hawthorne, F. C., Oberti, R., Harlow, G. E., Maresch, W. V., Martin, R. F., Schumacher, J. C., & Welch, M. D. (2012). IMA report nomenclature of the amphibole supergroup. *American Mineralogist*, 97(11–12), 2031–2048. <https://doi.org/10.2138/am.2012.4276>
- Henry, C. (1990). *L'unité a coésite du massif Dora-Maira dans son cadre pétrologique et structural (Alpes occidentales, Italie)*. PhD thesis. University of Paris. <https://hal.archives-ouvertes.fr/tel-03511047/>
- Henry, C., Michard, A., & Chopin, C. (1993). Geometry and structural evolution of ultra-highpressure and highpressure rocks from the Dora-Maira massif, Western Alps, Italy. *Journal of Structural Geology*, 15(8), 965–981. [https://doi.org/10.1016/0191-8141\(93\)90170-F](https://doi.org/10.1016/0191-8141(93)90170-F)
- Herron, M. M. (1988). Geochemical classification of terrigenous sands and shales from core or log data. *Journal of Sedimentary Petrology*, 58(5), 820–829. <https://doi.org/10.1306/212F8E77-2B24-11D7-8648000102C1865D>
- Holland, T. J. B., & Powell, R. (1998). An internally-consistent thermodynamic dataset for phases of petrological interest. *Journal of Metamorphic Geology*, 16, 309–344. <https://doi.org/10.1111/j.1525-1314.1998.00140.x>
- Holland, T. J. B., & Powell, R. (2011). An improved and extended internally consistent thermodynamic dataset for phases of petrological interest, involving a new equation of state for solids. *Journal of Metamorphic Geology*, 29, 333–383. <https://doi.org/10.1111/j.1525-1314.2010.00923.x>
- Holyoke, C. W., & Tullis, J. (2006). Formation and maintenance of shear zones. *Geology*, 34, 105–108. <https://doi.org/10.1130/G22116.1>
- Jamtveit, B., Malthe-Sørensen, A., & Kostenko, O. (2008). Reaction enhanced permeability during retrogressive metamorphism. *Earth and Planetary Science Letters*, 267, 620–627. <https://doi.org/10.1016/j.epsl.2007.12.016>
- Lanari, P., & Engi, M. (2017). Local bulk composition effects on metamorphic mineral assemblages. *Reviews in Mineralogy and Geochemistry*, 83, 55–102. <https://doi.org/10.2138/rmg.2017.83.3>
- Lanari, P., Vidal, O., De Andrade, V., Dubacq, B., Lewin, E., Grosch, E. G., & Schwartz, S. (2014). XMapTools: A MATLAB®-based program for electron microprobe X-ray image processing and geothermobarometry. *Computers & Geosciences*, 62, 227–240. <https://doi.org/10.1016/j.cageo.2013.08.010>
- Law, R. D. (2014). Deformation thermometry based on quartz c-axis fabrics and recrystallization microstructures: A review. *Journal of Structural Geology*, 66, 129–161. <https://doi.org/10.1016/j.jsg.2014.05.023>
- Le Bayon, B., & Ballèvre, M. (2006). Deformation history of a subducted continental crust (gran Paradiso, Western Alps): Continuing crustal shortening during exhumation. *Journal of Structural Geology*, 28(5), 793–815. <https://doi.org/10.1016/j.jsg.2006.02.009>
- Liou, J. G., & Zhang, R.-Y. (2002). Ultrahigh-pressure metamorphic rocks. *Encyclopaedia of Physical Science and Technology*, 17, 227–244. <https://doi.org/10.1016/B0-12-227410-5/00795-X>
- Luisier, C., Ballèvre, M., & Duret, T. (2023). The role of H<sub>2</sub>O on metamorphism and deformation at high pressure: A combined petrological and thermo-mechanical study based on the gran Paradiso unit, Western Alps. *Lithos*, 446–447, 107123. <https://doi.org/10.1016/j.lithos.2023.107123>
- Mancktelow, N. S. (2006). How ductile are ductile shear zones? *Geology*, 34, 345–348. <https://doi.org/10.1130/G22260.1>
- Manzotti, P., Ballèvre, M., & Poujol, M. (2016). Detrital zircon geochronology in the Dora-Maira and Zone Houillère: A record of sediment travel paths in the carboniferous. *Terra Nova*, 28(4), 279–288. <https://doi.org/10.1111/ter.12219>
- Manzotti, P., Poujol, M., & Ballèvre, M. (2015). Detrital zircon geochronology in blueschist-facies meta-conglomerates from the Western Alps: Implications for the late carboniferous to early Permian palaeogeography. *International Journal of Earth Sciences*, 104(3), 703–731. <https://doi.org/10.1007/s00531-014-1104-8>
- Manzotti, P., Schiavi, F., Nosenzo, F., Pitra, P., & Ballèvre, M. (2022). A journey towards the forbidden zone: A new, cold, UHP unit in the Dora-Maira massif (Western Alps). *Contributions to Mineralogy and Petrology*, 177, 59. <https://doi.org/10.1007/s00410-022-01923-8>
- McCaig, A. M., Wickham, S. M., & Taylor, H. P. (1990). Deep fluid circulation in alpine shear zones, Pyrenees, France: Field and oxygen isotope studies. *Contributions to Mineralogy and Petrology*, 106, 41–60. <https://doi.org/10.1007/BF00306407>
- Menegon, L., Fusses, F., Stünitz, H., & Xiao, X. (2015). Creep cavitation bands control porosity and fluid flow in lower crustal shear zones. *Geology*, 43(3), 227–230. <https://doi.org/10.1130/G36307.1>
- Merlo, C., & Malaroda, S. R. (1990). Il Complesso Carbonifero del Pinerolese (Zona Dora-Maira) nella Val Lemina (Pinerolo). *Rendiconti Lincei*, 1(1), 3–13. <https://doi.org/10.1007/BF03001744>
- Mertz, J. D., & Siddans, A. W. B. (1985). Finite strain states, quartz textures and the significance of lineation in permo-carboniferous metasediments of the Dora Maira massif, Val



- Germanasca, Italy. *Tectonophysics*, 118(1–2), 61–73. [https://doi.org/10.1016/0040-1951\(85\)90155-6](https://doi.org/10.1016/0040-1951(85)90155-6)
- Michard, A. (1967). *Etudes géologiques dans les zones internes des Alpes Cottiniennes*. CNRS. 420 pp., 25 plates, 10 fold-up. <https://tel.archives-ouvertes.fr/tel-00802836>
- Michard, A., Henry, C., & Chopin, C. (1993). Compression versus extension in the exhumation of the Dora-Maira coesite-bearing unit, Western Alps, Italy. *Tectonophysics*, 221(2), 173–193. [https://doi.org/10.1016/0040-1951\(93\)90331-D](https://doi.org/10.1016/0040-1951(93)90331-D)
- Michard, A., Henry, C., & Chopin, C. (1995). Structures in UHPM rocks: A case study from the Alps. In R. G. Coleman & X. Wang (Eds.), *Ultrahigh pressure metamorphism* (pp. 132–158). Cambridge University Press. <https://doi.org/10.1017/CBO9780511573088.005>
- Michard, A., Schmid, S. M., Lahfid, A., Ballèvre, M., Manzotti, P., Chopin, C., Iaccarino, S., & Dana, D. (2022). The Maira-Sampeyre and Val grana allochthons (South Western Alps): Review and new data on the tectonometamorphic evolution of the Briançonnais distal margin. *Swiss Journal of Geosciences*, 115(1), 19. <https://doi.org/10.1186/s00015-022-00419-8>
- Milke, R., Neusser, G., Kolzer, K., & Wunder, B. (2013). Very little water is necessary to make a dry solid silicate system wet. *Geology*, 41, 247–250. <https://doi.org/10.1130/G33674.1>
- Nerone, S., Groppo, C., & Rolfo, F. (2023). Equilibrium and kinetic approaches to understand the occurrence of the uncommon chloritoid + biotite assemblage. *European Journal of Mineralogy*, 35, 305–320. <https://doi.org/10.5194/ejm-35-305-2023>
- Nosenzo, F., Manzotti, F., & Robyr, M. (2023). H<sub>2</sub>O budget and metamorphic re-equilibration in polycyclic rocks as recorded by garnet textures and chemistry. *Lithos*, 452–453, 107230. <https://doi.org/10.1016/j.lithos.2023.107230>
- Nosenzo, F., Manzotti, P., Poujol, M., Ballèvre, M., & Langlade, J. (2022). A window into an older orogenic cycle: P–T conditions and timing of the pre-Alpine history of the Dora-Maira massif (Western Alps). *Journal of Metamorphic Geology*, 40, 789–821. <https://doi.org/10.1111/jmg.12646>
- Oliot, E., Goncalves, P., Schulmann, K., Marquer, D., & Lexa, O. (2014). Mid-crustal shear zone formation in granitic rocks: Constraints from quantitative textural and crystallographic preferred orientations analyses. *Tectonophysics*, 612–613, 63–80. <https://doi.org/10.1016/j.tecto.2013.11.032>
- Passchier, C. W., & Trouw, R. A. J. (2005). *Microtectonics* (p. 366). Springer. <https://doi.org/10.1007/3-540-29359-0>
- Pennacchioni, G., & Cesare, B. (1997). Ductile-brittle transition in pre-Alpine amphibolite facies mylonites during evolution from water-present to water-deficient conditions (Mont Mary nappe, Italian Western Alps). *Journal of Metamorphic Geology*, 15(6), 777–791. <https://doi.org/10.1111/j.1525-1314.1997.00055.x>
- Petroccia, A., Carosi, R., Montomoli, C., Iaccarino, S., & Vitale Brovarone, A. (2022). Deformation and temperature variation along thrust-sense shear zones in the hinterland-foreland transition zone of collisional settings: A case study from the Barbagia thrust (Sardinia, Italy). *Journal of Structural Geology*, 161, 104640. <https://doi.org/10.1016/j.jsg.2022.104640>
- Petroccia, A., & Iaccarino, S. (2021). Metaconglomerate in the Pine-rolo unit (Dora Maira massif, Western Alps): A key outcrop for Alpine geology and training structural geologists. *International Journal of Earth Sciences*, 111(1), 317–319. <https://doi.org/10.1007/s00531-021-02087-9>
- Piana, F., Fioraso, G., Irace, A., d'Atri, A., Barale, L., Falletti, P., Monegato, G., Morelli, M., Tallone, S., & Vigna, G. B. (2017). Geology of Piemonte region (NW Italy, Alps–Apennines interference zone). *Journal of Maps*, 13(2), 395–405. <https://doi.org/10.1080/17445647.2017.1316218>
- Powell, R., Guiraud, M., & White, R. W. (2005). Truth and beauty in metamorphic phase-equilibria: Conjugate variables and phase diagrams. *The Canadian Mineralogist*, 43, 21–33. <https://doi.org/10.2113/gscanmin.43.1.21>
- Proyer, A. (2003). The preservation of high-pressure rocks during exhumation: Metagranites and metapelites. *Lithos*, 70(3–4), 183–194. [https://doi.org/10.1016/S0024-4937\(03\)00098-7](https://doi.org/10.1016/S0024-4937(03)00098-7)
- Rubie, D. C. (1986). The catalysis of mineral reactions by water and restrictions on the presence of aqueous fluid during metamorphism. *Mineralogical Magazine*, 50(357), 399–415. <https://doi.org/10.1180/minmag.1986.050.357.05>
- Sandrone, R., & Borghi, A. (1992). Zoned garnets in the northern Dora-Maira massif and their contribution to a reconstruction of the regional metamorphic evolution. *European Journal of Mineralogy*, 4, 465–474. <https://doi.org/10.1127/ejm/4/3/0465>
- Sandrone, R., Cadoppi, P., Sacchi, R., & Vialon, P. (1993). The Dora-Maira Massif. In J. F. von Raumer (Ed.), *Pre-Mesozoic geology in the Alps* (pp. 317–325). Springer. [https://doi.org/10.1007/978-3-642-84640-3\\_18](https://doi.org/10.1007/978-3-642-84640-3_18)
- Schmid, S. M., & Kissling, E. (2000). The arc of the western Alps in the light of geophysical data on deep crustal structure. *Tectonics*, 19(1), 62–85. <https://doi.org/10.1029/1999TC900057>
- Schmid, S. M., Kissling, E., Diehl, T., van Hinsbergen, D. J., & Molli, G. (2017). Ivrea mantle wedge, arc of the Western Alps, and kinematic evolution of the Alps–Apennines orogenic system. *Swiss Journal of Geosciences*, 110(2), 581–612. <https://doi.org/10.1007/s00015-016-0237-0>
- Simonetti, M., Carosi, R., Montomoli, C., Law, R. D., & Cottle, J. M. (2021). Unravelling the development of regional-scale shear zones by a multidisciplinary approach: The case study of the Ferriere-Mollières shear zone (Argentera massif, Western Alps). *Journal of Structural Geology*, 149, 104399. <https://doi.org/10.1016/j.jsg.2021.104399>
- Spruzeniece, L., & Piazolo, S. (2015). Strain localization in brittle-ductile shear zones: Fluid-abundant vs. fluid-limited conditions (an example from Wyangala area, Australia). *Solid Earth*, 6(3), 881–901. <https://doi.org/10.5194/se-6-881-2015>
- Steffen, K., Selverstone, J., & Brearley, A. (2001). Episodic weakening and strengthening during synmetamorphic deformation in a deep-crustal shear zone in the Alps. *Geological Society, London, Special Publications*, 186(1), 141–156. <https://doi.org/10.1144/GSL.SP.2001.186.01.09>
- Stipp, M., Stünitz, H., Heilbron, M., & Schmid, D. W. (2002). The eastern tonale fault zone: A natural laboratory for crystal plastic deformation of quartz over a temperature range from 250 to 700 °C. *Journal of Structural Geology*, 24, 1861–1884. [https://doi.org/10.1016/S0191-8141\(02\)00035-4](https://doi.org/10.1016/S0191-8141(02)00035-4)
- Stipp, M., Tullis, J., Scherwath, M., & Behrmann, J. H. (2010). A new perspective on paleopiezometry: Dynamically

- recrystallized grain size distributions indicate mechanism changes. *Geology*, 38(8), 759–762. <https://doi.org/10.1130/G31162.1>
- Tenczer, V., Powell, R., & Stüwe, K. (2006). Evolution of H<sub>2</sub>O content in a polymetamorphic terrane: The Plattengneiss shear zone (Koralpe, Austria). *Journal of Metamorphic Geology*, 24, 281–295. <https://doi.org/10.1111/j.1525-1314.2006.00637.x>
- Thompson, A. B. (1983). Fluid-absent metamorphism. *Journal of the Geological Society*, 140(4), 533–547. <https://doi.org/10.1144/gsjgs.140.4.0533>
- Tursi, F. (2022). The key role of  $\mu\text{H}_2\text{O}$  gradients in deciphering microstructures and mineral assemblages of mylonites: Examples from the Calabria polymetamorphic terrane. *Mineralogy and Petrology*, 116, 1–14. <https://doi.org/10.1007/s00710-021-00766-8>
- Tursi, F., Acquafredda, P., Festa, V., Fornelli, A., Langone, A., Micheletti, F., & Spiess, R. (2021). What can high-*P* sheared orthogneisses tell us? An example from the Curinga–Girifalco line (Calabria, southern Italy). *Journal of Metamorphic Geology*, 39(7), 919–944. <https://doi.org/10.1111/jmg.12596>
- Tursi, F., Festa, V., Fornelli, A., Micheletti, F., & Spiess, R. (2018). Syn-shearing mobility of major elements in ductile shear zones: State of the art for felsic deformed protoliths. *Periodico di Mineralogia*, 87(3), 289–308. <https://doi.org/10.2451/2018PM811>
- Tursi, F., Spiess, R., Festa, V., & Fregola, R. A. (2020). Hercynian subduction-related processes within the metamorphic continental crust in Calabria (southern Italy). *Journal of Metamorphic Geology*, 38(7), 771–793. <https://doi.org/10.1111/jmg.12537>
- Ulmer, P. (1986). *NORM - program for cation and oxygen mineral norms*. Computer Library, Institut für Mineralogie und Petrographie, ETH-Zentrum, ETH-Zentrum.
- Vaughan-Hammon, J. D., Candioti, L. G., Duretz, T., & Schmalhotz, S. M. (2022). Metamorphic facies distribution in the Western Alps predicted by petrological-thermomechanical models of Syn-convergent exhumation. *Geochemistry, Geophysics, Geosystems*, 23(8), e2021GC009898. <https://doi.org/10.1029/2021GC009898>
- Vialon, P. (1966). *Étude géologique du Massif Cristallin Dora-Maira (Alpes Cottiennes internes-Italie)*. PhD thesis (p. 293). University of Grenoble. <https://tel.archives-ouvertes.fr/tel-00723197>
- Warr, L. N. (2021). IMA–CNMNC approved mineral symbols. *Mineralogical Magazine*, 85, 291–320. <https://doi.org/10.1180/mgm.2021.43>
- Wheeler, J. (1991). Structural evolution of a subducted continental sliver - the northern Dora Maira massif, Italian Alps. *Journal of the Geological Society*, 148, 1101–1113. <https://doi.org/10.1144/gsjgs.148.6.1101>
- Wheeler, J. (2014). Dramatic effects of stress on metamorphic reactions. *Geology*, 42, 647–650. <https://doi.org/10.1130/G35718.1>
- White, R. W., Powell, R., & Johnson, T. E. (2014). The effect of Mn on mineral stability in meta-pelites revisited: New a-x relations for manganese-bearing minerals. *Journal of Metamorphic Geology*, 32, 809–828. <https://doi.org/10.1111/jmg.12095>
- Yardley, B. W. D., Rhede, D., & Heinrich, W. (2014). Rates of retrograde metamorphism and their implications for the rheology of the crust: An experimental study. *Journal of Petrology*, 55(3), 623–641. <https://doi.org/10.1093/petrology/egu001>

## SUPPORTING INFORMATION

Additional supporting information can be found online in the Supporting Information section at the end of this article.

**Figure S1:** Bulk chemical classification SandClass3 of Herron (1988), where sample BAR-4B protolith plots in the shale field, not far from the Worldwide Average Pelite (Forshaw & Pattison, 2023), while sample BAR-8 protolith plots in the lith-arenite field.

**Figure S2:** Garnet chemical variation and zoning profile highlighting the different shells, i.e., core, mantle and rim.

**Figure S3:** Explorative *P*–*X* (Fe<sub>2</sub>O<sub>3</sub>) phase diagram at fixed *T* for sample BAR-8 to test if epidote needs to be included in the bulk rock composition.

**Figure S4:** Isochemical phase diagram for BAR-4B with Bulk II to test if a fixed H<sub>2</sub>O content, i.e., 3.13 wt% from peak *P*–*T* conditions, can be considered to model the retrograde phase relations.

**Supplementary Information S1:** Phase relation summary combining microstructural observation and chemical composition of the phases.

**Table S1:** Synoptic table reporting the central-southern Dora-Maira Massif subdivision and *P*–*T* data available from the literature.

**Table S2:** Complete dataset of mineral chemical analysis for sample BAR-4B.

**Table S3:** Complete dataset of mineral chemical analysis for sample BAR-8.

**Table S4:** *P*/*T* equations used for the *P*/*T*–MH<sub>2</sub>O investigation.

**How to cite this article:** Nerone, S., Petroccia, A., Caso, F., Dana, D., & Maffei, A. (2024). Assessing the importance of H<sub>2</sub>O content in the tectono-metamorphic evolution of shear zones: A case study from the Dora-Maira Massif (Western Alps). *Journal of Metamorphic Geology*, 42(2), 171–196. <https://doi.org/10.1111/jmg.12750>